Multicriteria optimization of Brayton-like pumped thermal electricity storage with liquid media

J. Gonzalez-Ayala [a,b,*], D. Salomone-González [c], A. Medina [a,b], J.M.M. Roco [a,b], P.L. Curto-Risso [c], A. Calvo Hernández [a,b]

[a] *Departamento de Física Aplicada, Universidad de Salamanca, 37008 Salamanca, Spain*
[b] *Instituto Universitario de Física Fundamental y Matemáticas (IUFFyM), Universidad de Salamanca, 37008 Salamanca, Spain*
[c] *Facultad de Ingeniería, Universidad de la República, Montevideo, Uruguay*

ARTICLE INFO

ABSTRACT

A multi-objective and multi-parametric optimization of a Pumped Thermal Electricity Storage system based on Brayton cycles is presented by the calculation of different Pareto fronts and the associated Pareto optimal sets for energetic and design analysis, respectively. A large range of internal and external irreversibilities and the thermodynamic properties of the storage media are taken into account. The analysis shows that the heat capacity of the working fluid and the heat capacity of the storage media should be the same in the contact with the hot reservoirs and in the contact with the cold reservoir in the heat pump, but in the contact with the cold reservoir for the heat engine the ratio should be 0.33, this offers information regarding the mass flow increasing significantly the achievable values for the round-trip efficiency, power output and the heat engine efficiency in the discharge process. Optimal values are given in terms of the degree of irreversibilities in the system and a comparison is made with extreme cases of infinite and minimum sizes for the storage system. Round-trip efficiencies in the so-called optimum scale/mass-flow-ratio design point exhibits noticeably larger values compared to previously reported results including the so-called endoreversible limit, where no internal irreversibilities are considered and where the improvement can achieve 49% over the endoreversible case in the most ideal scenario. Explicit numerical values of the maximum round trip efficiency, power output, and efficiency are given for a broad range of both internal and external irreversibilities.

1. Introduction

Electric energy storage technology based on the joint use of a heat pump and a heat engine cycles (pumped thermal electricity storage, PTES) is nowadays a real alternative to most conventional technologies as compressed air energy storage (CAES) or pumped hydro storage (PHS) [1]. It does not require neither underground caves nor high-sized reservoirs and then, it is not dependent on geographic or geological conditions [2]. In PTES devices energy is stored in the form of heat in a hot tank with manageable dimensions using a heat pump (HP)-cycle which extracts heat from a lower temperature tank containing a cryogenic liquid [3]. Later-on, the energy stored (in molted salts [4], for example) is converted into electric energy in a discharge process through a heat engine (HE) cycle working between the same thermal energy storage (TES) media [5].

Compared with solid media storage [6], two clear additional advantages of the liquid storage are: (a) the pressure inside the tanks is independent of the pressure of the cyclic working fluid (opposite to

what happens in packed bed storage systems) and then, more compact heat exchangers can be used; and (b) the temperature inside each tank remains almost constant, avoiding the problems associated to the propagation of the hot front in solid storage [7,8]. The drawback is the need for two tanks for each reservoir with specific technical requirements [9] (high volumetric specific energy, high heat rate with the working fluid, high thermal stability, flexibility for implementation, storage capacity for hours of operation, and long lifetime). For the cryogenic fluids [10] and the storage salts [11], lower and upper limits in the temperature should be taken into account [12] in order to ensure stable liquid phases under the whole cyclic working fluid temperature variations [13] .

PTES layouts [14], even those with de-coupled thermal stores [15] and unbalanced mass flow rate [16], mostly uses a single-phase working fluid operating a Brayton-like [17] cycle or Rankine-like cycle [18] with CO_2 as working fluid [19]. Most of full theoretical studies are

Nomenclature

a	Temperature ratio
c_p	Specific heat capacity at constant pressure (J/kg K)
c_v	Specific heat capacity at constant volume (J/kg K)
C	Heat capacity (W/K)
k	Dimensionless factor $\left(\frac{\gamma-1}{\gamma}\right)$
$\dot{m}$	Mass flow (kg/s)
p	Pressure (atm)
$\dot{Q}$	Heat flow (W)
r	Pressure ratio
T	Temperature (K)
P_{out}	Power output (W)
$\bar{P}_{out}$	Especific power ($P_{out}/\dot{m}C$ (K))
Y	Dimensionless factors
Z	Dimensionless factors

Greek Letters

γ	Adiabatic coefficient
Γ	Dimensionless factor
ϵ	Efficiencies
η	Efficiency of the heat engine
ν	COP of the heat pump
ξ	Heat leak factor
ρ	Pressure drop coefficient
Φ	Round trip efficiency

Subscript

c	Compressor
H	High pressure
L	Low pressure
t	Turbine
w	Working fluid

Acronyms

COP	Coefficient of performance
HE	Heat engine
HP	Heat pump
$PTES$	Pumped thermal electricity storage
RTE	Round trip efficiency
TES	Thermal energy storage

based on finite-time thermodynamic frameworks [20] assuming Carnot-like models [21], weakly-dissipative models [22], and/or Brayton-like cycles [23]. All these thermodynamic models assume constant temperatures for TES systems so that they are amenable to analytical expressions for the main involved energetic magnitudes (as maximum power, maximum round trip efficiency, maximum COP) and/or trade-off figures of merit. Also comparison with performance optimization [24] and optimized round-trip efficiencies [25] of cryogenic electricity storage system and advanced exergy analysis have been recently published [26].

Although theoretical parametric studies provide physical basis for guiding pre-design of main energetic magnitudes, a full optimization of the overall system for a selected salt and cryogenic medium remains a complex task due to three main points [27]: (a) the large number of operational and design parameters; (b) the trade-off objectives (e.g. round trip efficiency, power output, heat pump COP, heat engine efficiency);

and (c) uncertainties in regards with both internal and external losses and heat leaks models. Robust numerical optimization algorithms are thus needed to identify promising and realistic designs and then, results of these analyses could better estimate the performance of individual subsystems and that of the entire device. Therefore a multi-objective and multi-parametric optimization is required to fully explore the PTES performance potentialities and limitations beyond pre-design thermodynamics results [28]. These algorithms provide trade-off surfaces (Pareto fronts) from which insights on how the optimal design (Pareto optimal sets) should vary when multiple objective are considered.

The main contribution of this paper is to find an optimal relation between the heat capacities of the working fluid and the thermal reservoirs. This can be tuned through the mass flow in the contact with the hot and cold reservoirs in both operation modes. Thus, an optimal design point was obtained by means of a multi-parametric optimization based on different trade-off figures of merit for a recently proposed steady-state PTES theoretical model based on Brayton-like cycles with non-constant temperature at the TES. The involved figures of merit are the round trip efficiency of the whole device, the power output and the efficiency of the discharge mode.

The paper is structured as follows. Section 2 summarizes a basic description of the HE and HP cycles as well as their coupling for the whole thermodynamic model. It is based on the previous study for the same model reported in [29] by coupling a Brayton heat pump and a Brayton heat engine. Section 3 firstly shows the technical aspects of the multi-criteria optimization methodology. The optimization is developed in three stages beginning with all the available parameters. Later on, it is shown that five of them allow for determining an optimal design point. In that configuration a final optimization is made. This is done focusing on round-trip efficiency Φ, power output P_{out}, and efficiency of the discharge process η, as those that exhibit convex behaviours. Special emphasis is paid on the role played by the internal and external irreversibilities as well as the size of the composed cycle. Explicit maximum values of Φ, P_{out} and η are given. Finally, in Section 4 a summary and the most relevant conclusions are outlined.

2. Thermodynamic model: background

The complete model for both the HE- and HP-operation was reported in a previous study mainly devoted to a thermodynamic assessment [29]. Here, only the main hypotheses and the role of the involved parameters are summarized .

2.1. Background

The proposed overall arrangement consists in a combination of a Brayton-like HP cycle followed by a Brayton-like HE cycle. In both operation modes, the liquid media is stored in four tanks at different constrained temperatures, in such a way that adequate integration profiles for the charge/discharge processes holds by counter-flow heat exchangers, whose temperatures are also affected by a small heat-leak that is taken into account.

Heat pump performance. Along the anti-clockwise charge process (see Fig. 1), the working fluid enters into the HP compressor at state 3 and after a non-isentropic compression (step $3 \rightarrow 2$) the working fluid reaches its maximum pressure and maximum temperature. Then, heat rejection by the working fluid, with a pressure drop $\Delta P_H = P_2 - P_1$, is used in the counter-flow heat exchanger to increase the temperature of the molten salt from T_{H2} to T_{H1} as the working fluid is cooled down along process $2 \rightarrow 1$. Next, the working fluid expands in a non-isentropic process $1 \rightarrow 4$ getting its lowest temperature and pressure. In the next step, the working fluid is slowly heated up by the heat flow coming from the cold liquid material initially at temperature T_{L2}. Then, the cold storage liquid diminishes its temperature to T_{L1} while the working fluid increases its temperature along step $4 \rightarrow 3$ with a pressure drop $\Delta P_L = P_4 - P_3$, recovering the initial state at temperature
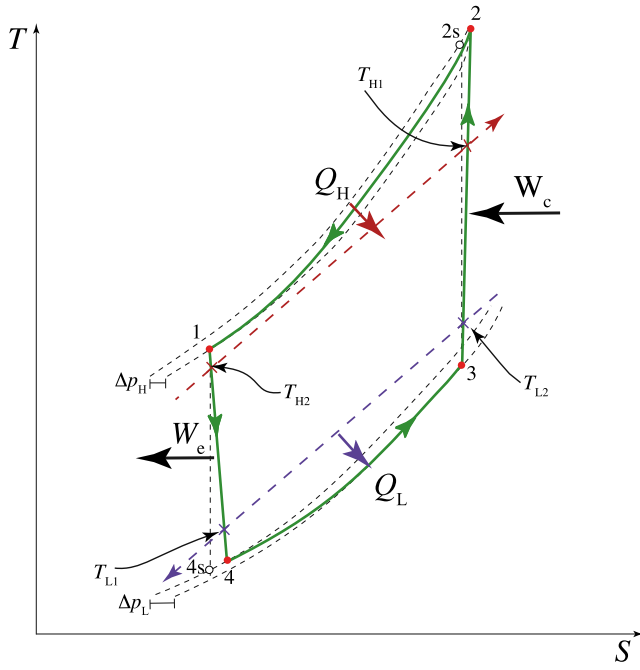
Fig. 1. $T-S$ setup of the charge HP cycle.

T_3 and pressure P_3. The relevant temperatures at the corners of the HP cycle are given by:

$$T_1 = \frac{T_{H2}\epsilon_H + T_{L2}Z_1\epsilon_L(1-\epsilon_H)}{1 - Z_1Z_2(1-\epsilon_H)(1-\epsilon_L)}, \tag{1}$$

$$T_3 = \frac{T_{L2}\epsilon_L + T_{H2}Z_2\epsilon_H(1-\epsilon_L)}{1 - Z_1Z_2(1-\epsilon_H)(1-\epsilon_L)}, \tag{2}$$

$$T_2 = T_3 Z_1, \tag{3}$$

$$T_4 = T_1 Z_2, \tag{4}$$

where

$$Z_1 \equiv \frac{a_c - (1-\epsilon_c)}{\epsilon_c}, \qquad Z_2 \equiv \frac{a_t(1-\epsilon_t)+\epsilon_t}{a_t}, \tag{5}$$

and the compression and expansion ratios, r_c and r_t, are linked to pressure drop coefficients ρ_H and ρ_L by

$$a_c \equiv \frac{T_{2s}}{T_3} = r_c^k = \left(\frac{P_2}{P_3}\right)^k = \left(\frac{P_2}{P_4 - \Delta P_L}\right)^k, \tag{6}$$

$$a_t \equiv \frac{T_1}{T_{4s}} = r_t^k = \left(\frac{P_1}{P_4}\right)^k = \left(\frac{P_2 - \Delta P_H}{P_4}\right)^k, \tag{7}$$

where $k = \frac{\gamma-1}{\gamma}$ and $\gamma = c_p/c_V$ is the adiabatic coefficient of the working fluid. In this way a_t and a_c are linked by the relation

$$a_t = \rho_H \rho_L a_c, \tag{8}$$

with

$$\rho_H = \left(\frac{P_1}{P_2}\right)^k = \left(\frac{P_2 - \Delta P_H}{P_2}\right)^k, \tag{9}$$

$$\rho_L = \left(\frac{P_3}{P_4}\right)^k = \left(\frac{P_4 - \Delta P_L}{P_4}\right)^k. \tag{10}$$

As usual and in order to account for internal losses at the compressor and turbine, isentropic efficiencies for the compression ϵ_c and expansion processes ϵ_t are used

$$\epsilon_c = \frac{T_{2s} - T_3}{T_2 - T_3}, \tag{11}$$

$$\epsilon_t = \frac{T_1 - T_4}{T_1 - T_{4s}}, \tag{12}$$

where T_{2s} and T_{4s} refer to ideal isentropic processes. The temperatures of the liquid media are calculated as:

$$T_{H2} = T_{H1} - \Gamma_H(T_2 - T_1), \tag{13}$$

$$T_{L2} = T_{L1} + \Gamma_L(T_3 - T_4), \tag{14}$$

where $\Gamma_H \equiv \frac{C_W}{C_H}$ and $\Gamma_L \equiv \frac{C_W}{C_L}$ are the ratios of the working fluid heat capacity per-unit-time ($C_w \equiv \dot{m}_w c_{pw}$) and the corresponding thermal reservoir ($C_{H,L} = \dot{m}_{H,L} c_{pH,L}$). These equations play an important role as they link the salt temperatures of the hot tanks (T_{H1} and T_{H2}) an of the cryogenic liquid (T_{L1} and T_{L2}) with the temperatures of the working fluid in the extreme states of the HP cycle in terms of dimensionless coefficients Γ_H and Γ_L.

In regards with the unavoidable heat leak between the hot and cold sides of the overall plant a full study is out of the scope of the present paper. Here it will be assumed only an indirect effect of a heat leak between the molten salt sources T_{H1} and T_{H2} with the environment at temperature T_0, and a negligible heat leak due to the cold liquid storage. In an average manner and according to empirical results [30], this effect is assumed as a linear decrease of the temperatures T_{H1} y T_{H2} with an effective proportionality factor ξ so that the initial temperatures T_{H1} y T_{H2} decrease due to heat leak as:

$$\Delta T_{H1} = -\xi(T_{H1} - T_0), \tag{15}$$

$$\Delta T_{H2} = -\xi(T_{H2} - T_0). \tag{16}$$

The heat leak in the molten salt that affects its temperature will not enter into the analysis of the efficiency. The input power on the working fluid by the compressor W_c and the power output W_t in the expander (turbine) are:

$$W_c = C_w(T_2 - T_3) = C_w T_3 \left(\frac{a_c - (1-\epsilon_c)}{\epsilon_c}\right), \tag{17}$$

$$W_t = C_w(T_1 - T_4) = C_w T_1 \epsilon_t \left(\frac{a_t - 1}{a_t}\right). \tag{18}$$

For the calculation of the heat rates $\dot{Q}_H$ and $\dot{Q}_L$, it is assumed a balance between the heat rates of the working fluid $C_w(T_2 - T_1)$ and $C_w(T_3 - T_4)$ and the heat rate in the hot and cold sides of the counter-flow heat exchangers $C_H(T_{H1} - T_{H2})$ and $C_L(T_{L2} - T_{L1})$ through global effectiveness ϵ_H and ϵ_L:

$$\dot{Q}_H = C_w(T_2 - T_1) = C_H(T_{H1} - T_{H2}) = C_{H,min}\epsilon_H(T_2 - T_{H2}), \tag{19}$$

$$\dot{Q}_L = C_w(T_3 - T_4) = C_L(T_{L2} - T_{L1}) = C_{L,min}\epsilon_L(T_{L2} - T_4), \tag{20}$$

where $C_{H,min} = min(C_H, C_w)$, $C_{L,min} = min(C_L, C_w)$ are the minimal heat capacities of the hot and cold TES media.

The COP ν of the heat pump cycle is thus calculated from $\nu \equiv \dot{Q}_H/(\dot{Q}_H - \dot{Q}_L)$.

Heat engine performance. Along the clockwise discharge process (see Fig. 2), the working fluid undergoes a non-isentropic compression $4 \to 1$; then it is heated, with a pressure drop $\Delta P_H = P_1 - P_2$, across the temperature gap $T_1 - T_2$ by the heat delivery in the counter-flow heat exchanger of the hot storage molten salt, which in turn decreases its temperature from T_{H1} to T_{H2}. Afterwards, the hot working fluid at T_2 is expanded in the non-isentropic turbine ($2 \to 3$), and finally, it is cooled to its initial temperature T_4 experiencing a pressure drop $\Delta P_L = P_3 - P_4$. The heat delivered in this step by the working fluid allows the increase of temperature of the cold liquid medium from T_{L1} to T_{L2} by means of the (cold) counter-flow heat exchanger. After the end of HE cycle and in order to recuperate the initial conditions of the HP cycle, a heat exchanger could be necessary for process $T_{3HE} \to T_{3HP}$. This feature is out of the scope of this work because of the steady state performance is only considered and transient behaviours are avoided.

In this case the extreme temperatures of the HE devices are:

$$T_2 = \frac{T_{H1}\epsilon_H + T_{L1}Y_1\epsilon_L(1-\epsilon_H)}{1 - Y_1Y_2(1-\epsilon_H)(1-\epsilon_L)}, \tag{21}$$
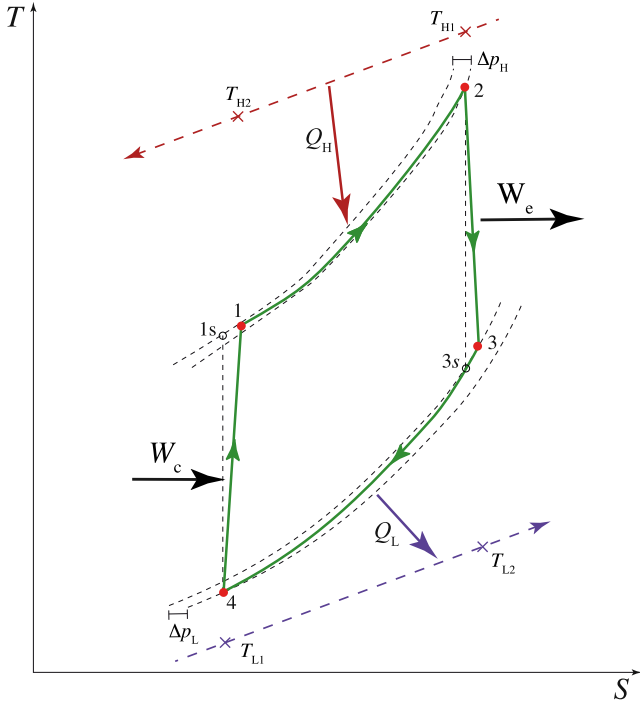
Fig. 2. $T - S$ setup of the discharge HE cycle.

$$T_4 = \frac{T_{L1}\epsilon_L + T_{H1}Y_2\epsilon_H(1-\epsilon_L)}{1 - Y_1Y_2(1-\epsilon_H)(1-\epsilon_L)}, \tag{22}$$

$$T_1 = T_4Y_1, \tag{23}$$

$$T_3 = T_2Y_2, \tag{24}$$

where

$$Y_1 \equiv \frac{a_c - (1-\epsilon_c)}{\epsilon_c}, \qquad Y_2 \equiv \frac{a_t(1-\epsilon_t)+\epsilon_t}{a_t}, \tag{25}$$

and

$$a_c \equiv \frac{T_{1s}}{T_4} = r_c^k = \left(\frac{P_1}{P_4}\right)^k = \left(\frac{P_1}{P_3 - \Delta P_L}\right)^k, \tag{26}$$

$$a_t \equiv \frac{T_2}{T_{3s}} = r_t^k = \left(\frac{P_2}{P_3}\right)^k = \left(\frac{P_1 - \Delta P_H}{P_3}\right)^k, \tag{27}$$

which are linked by the same relation than in the HP cycle

$$a_t = \rho_H\rho_L a_c. \tag{28}$$

with pressure drop coefficients

$$\rho_H = \left(\frac{P_2}{P_1}\right)^k = \left(\frac{P_1 - \Delta P_H}{P_1}\right)^k, \tag{29}$$

$$\rho_L = \left(\frac{P_4}{P_3}\right)^k = \left(\frac{P_3 - \Delta P_L}{P_3}\right)^k, \tag{30}$$

and isentropic efficiencies

$$\epsilon_c = \frac{T_{1s}-T_4}{T_1-T_4}, \tag{31}$$

$$\epsilon_t = \frac{T_2-T_3}{T_2-T_{3s}}. \tag{32}$$

The temperatures of the salt tanks (T_{H2}, T_{H1}) and of the cryogenic liquid (T_{L2} and T_{L1}) in terms of the corresponding dimensionless coefficients Γ_H and Γ_L are given as:

$$T_{H1} = T_{H2} + \Gamma_H(T_2 - T_1), \tag{33}$$

$$T_{L1} = T_{L2} - \Gamma_L(T_3 - T_4), \tag{34}$$

with $\Gamma_H \equiv \frac{C_W}{C_H}$ and $\Gamma_L \equiv \frac{C_W}{C_L}$.

In the HE mode the high temperature liquid store decreases its temperature from T_{H1} to T_{H2} as the working fluid temperature increases from T_1 to T_2 while absorbing heat through the heat exchanger. Opposite to this, the low temperature store increases its temperature from T_{L1} to T_{L2} as the working fluid temperature decreases from T_3 to T_4 while delivering heat through the heat exchanger. As for the HP-cycle, these heat transfers can be written in terms of the effectiveness as:

$$\dot{Q}_H = C_w(T_2 - T_1) = C_H(T_{H1} - T_{H2}) = C_{H,min}\epsilon_H(T_{H1} - T_1) \tag{35}$$

$$\dot{Q}_L = C_w(T_3 - T_4) = C_L(T_{L2} - T_{L1}) = C_{L,min}\epsilon_L(T_3 - T_{L1}) \tag{36}$$

which links the temperatures of the hot tanks (T_{H1} and T_{H2}) and the cryogenic liquid (T_{L1} and T_{L2}) with the temperatures of the working fluid in the extreme states of the HE cycle

For the heat leak same assumptions as for the HP cycle are accounted for, i.e., a linear decrease of the temperatures T_{H1} y T_{H2} with a proportionality factor ξ is considered:

$$\Delta T_{H1} = -\xi(T_{H1} - T_0), \tag{37}$$

$$\Delta T_{H2} = -\xi(T_{H2} - T_0). \tag{38}$$

From the above equations, the efficiency of the Brayton heat engine in the discharge phase, is calculated as $\eta = \dot{W}_{out}/\dot{Q}_H = (\dot{Q}_H - \dot{Q}_L)/\dot{Q}_H$.

Overall performance. In Fig. 3 a sketch of the $T - S$ diagram of both HP and HE cycles is depicted. The overall performance of the PTES system is defined in terms of the usual steady-state round trip efficiency, Φ, defined as:

$$\Phi = \frac{\dot{W}_{out}^{HE}}{\dot{W}_{net}^{HP}} = \frac{\eta \dot{Q}_H^{HE}}{\nu^{-1}\dot{Q}_H^{HP}} \tag{39}$$

In specific cases the difference between T_{H2}^{HP} and T_{H2}^{HE} is significant (see Fig. 3). In those cases heat should be extracted form the reservoir before starting the subsequent charging stage. This allows to include a secondary system, but this issue will not be addressed within the present paper.

2.2. Performance parameters and constraints

The thermodynamic model incorporates internal irreversibilities coming from non-isentropic expansion and compression processes in the turbine (expander) and compressor, respectively, and from pressure drops in the heater and in the cooler processes. The model also incorporates heat leak to the environment coming from the hot molten salt (not shown in Figs. 1 and 2) while heat leak from the liquid cold storage is assumed to be negligible, which is a reasonable assumption at least for short operation times.

The compression ratios, r_c^{HE} and r_c^{HP}, the adiabatic coefficient (γ) of the working fluid and the dimensionless coefficients $\Gamma_H^{HE} = C_w/C_H$, $\Gamma_L^{HE} = C_w/C_L$ for the discharging mode and $\Gamma_H^{HP} = C_w/C_H$, $\Gamma_L^{HP} = C_w/C_L$ for the charging cycle, are the fundamental variables in the resulting cycle geometry. The remaining parameters are classified according to irreversibilities:

(a) internal irreversibilities: accounted for the isentropic efficiencies, ϵ_c and ϵ_t, and the pressure drop coefficients in the high and low temperature sides (ρ_H, ρ_L).

(b) external irreversibilities: accounted for the heat leak parameter, ξ, and the parameters for the coupling of the working fluid to the external liquid media, ϵ_H and ϵ_L.

Additionally, a constraint in which $Q_h^{HE} \leq Q_h^{HP}$ is considered. It is common in the literature to fix the relation between this two quantities, but in this work this constraint is relaxed. This results in different behaviours when optimizing the round-trip efficiency (in which case the equality is *preferred*) and when optimizing η (in which case the equality is not preferred). The main constraint to link both engines is that the temperatures $T_{H1}^{HE} = T_{H2}^{HP}$, this after the effects of the heat-leak.
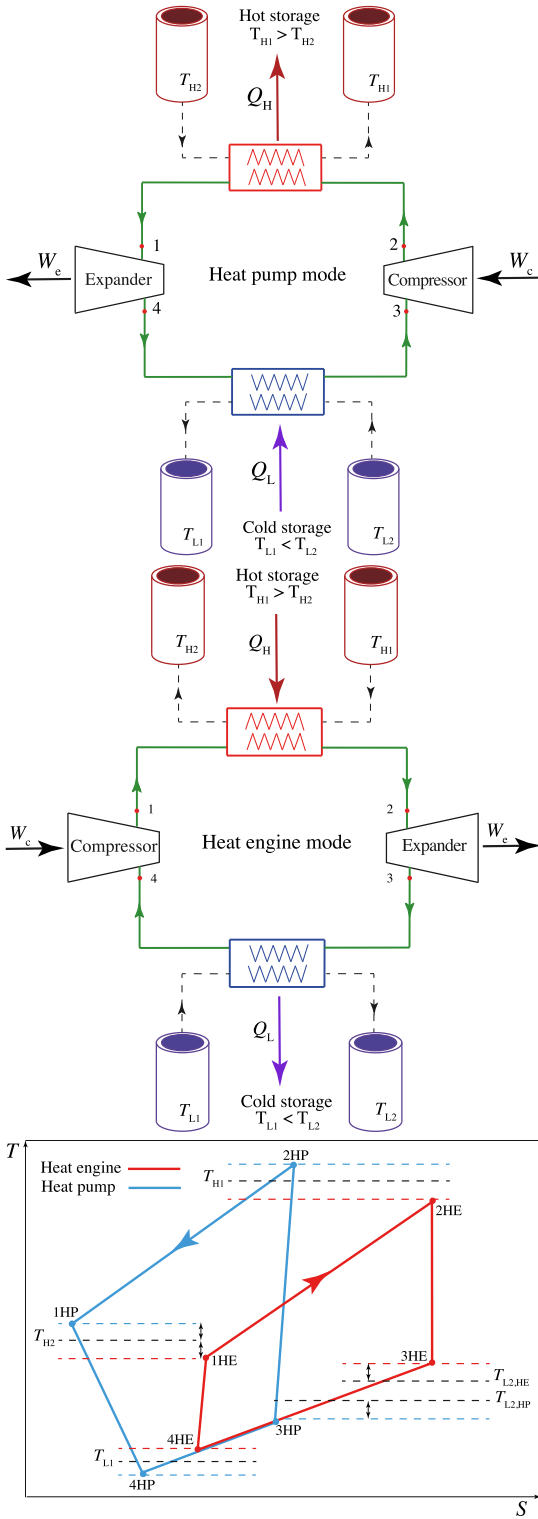
Fig. 3. The HP and HE layouts are depicted along with the setup of the whole thermodynamic cycle for the PTES system in the $T-S$ space.

Concerning with the TES liquid media temperatures, some restrictions should be taken into account to keep the liquid nature of the salt and of the cryogenic medium. These features impose some corresponding bounds in the values of T_{H1}, T_{H2}, T_{L1}, and T_{L2} in such a way that $T_{H2} \geq T_{min,salt}$, $T_{H1} \leq T_{max,salt}$ with $T_{min,salt}$ and $T_{max,salt}$ being, respectively, the melting and stability temperature of the salt and $T_{L1} \geq$

Table 1
Some thermal properties of the solar salt and cryogenic liquid considered for the analysis. T_{min} represents the melting point or approximate liquidus point for the TES medium. T_{max} the thermal stability temperature for the salt and the boiling temperature for the cryogenic liquid. Heat capacity c_p and density ρ. All these properties are assumed as constant [11].

Liquid (reservoirs)	T_{min} (K)	T_{max} (K)	c_p (kJ/kg K)	ρ (kg/l)
Solar salt	511	858	1.55	1.71
Anhydrous methanol	175.3	337.5	2.55	0.787

$T_{min,cry}$, $T_{L2} \leq T_{max,cry}$ with $T_{min,cry}$ and $T_{max,cry}$ being, respectively, the melting and boiling temperature of the cryogenic liquid storage. In the subsequent analysis the representative case of Ar as working fluid ($\gamma = 1.667$) with Solar Salt as storage medium and anhydrous methanol as the cryogenic substance.

3. Multiobjective and multiparametric optimization

Two main problems are faced here. First, it is not possible to provide a theoretical simultaneous optimization of all the relevant thermodynamic functions. Instead of optimizing the several possible functions separately, it is of interest to search for the so-called Pareto front, which gives the best performance when looking to simultaneously optimize a number of objective functions [31]. A second and more intricate issue, as it was showed in a previous work [29], is the set of possible values that the thermodynamic functions may have according to a variety of physical considerations. It is pointed out that the properties of the cryogenic and molten salts materials impose strong constraints regarding the highest and lower temperature values of the working fluid in the Brayton arrangement. Additionally, for some configurations of the system parameters, certain regimes might not be achievable since the physical acceptable regions in the thermodynamic space depend on the specific combinations of parameters. Thus, a set of physical constraints (no heat fluxes should reverse direction, positive input/output power and physical ranges in the efficiency, COP and round trip efficiency) determine the feasible coupling of both the HE and HP cycles. Information on this will be obtained from the Pareto optimal set. The resulting value of the eighteen parameters stemming from irreversibilities and design geometry should be tackled by multiobjective and multiparametric optimization.

3.1. Technical background

The basic idea of multiobjective optimization relies on the concept of dominance. The goal of this framework is to determine the Pareto optimal set (in the parameters space) and their corresponding Pareto front (in the energetic space).

The usual concept of dominance is the following: a vector $v = (v_1, \ldots, v_n)$ dominates another one $w = (w_1, \ldots, w_n)$ if and only if $v_i \geq w_i \; \forall \, i \in \{1, \ldots, n\}$ (for the maximum, $\leq$ for the minimum) and there is at least one j such that $v_j > w_j$. In other words, there are no other vectors having a better values in all entries. The algorithm presented here it is a modification of the one introduced in [32,33], and is as follows:

1. The phase space is defined from the operation variables a_c^{HE} and a_c^{HP} (which define the operation regime). Also, the phase space includes the rest of the parameters: internal irreversibilities are accounted by $\{\epsilon_c, \epsilon_t, \rho_H, \rho_L\}$, external irreversibilities are modelled through $\{\epsilon_H, \epsilon_L, \xi\}$, and $\{\Gamma_L, \Gamma_H\}$ are related with the mass flow (or size) of the device according to the mass flow (or size) of the external heat reservoirs. Eighteen parameters in total accounting for the HE and the HP (leaving open the possibility of having separate devices) determine the range of possible values of a_c^{HE} and a_c^{HP}.
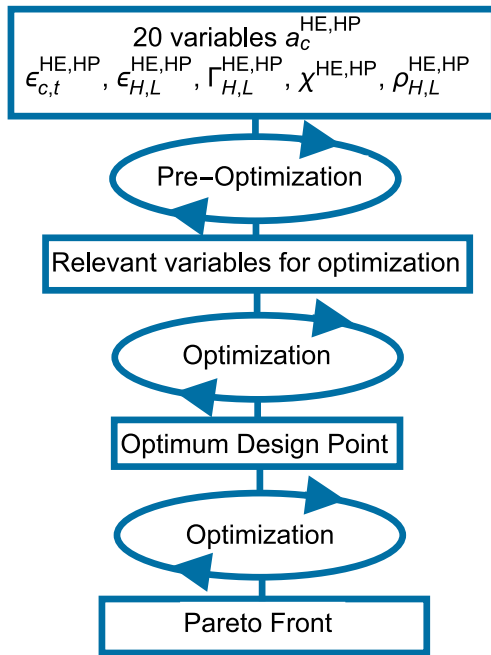
Fig. 4. Optimization scheme. First, relevant parameters are determined. In a second stage an optimum design point is found and finally, the Pareto front is obtained.

2. The region of physical relevance in the phase space is defined ($P > 0$, $P_{in} > 0$, $\eta > 0$, $\Phi \in [0, 1]$, $\nu > 1$. Moreover, all heat fluxes should have the correct sign).

3. From this region a random set of points in the phase space is obtained and the thermodynamic functions are evaluated (energetic space).

4. The set of non-dominated points in the energetic space is obtained, resulting in a provisional Pareto front.

5. From the corresponding Pareto optimal set (phase space) a cover (cubic region) is defined and extended in order to encompass a larger region for searching new points in the Pareto front.

6. From the new region a new set of random points is proposed and a new set of non-dominated points in the energetic space is obtained. As the algorithm is iterated the output is closer to the true Pareto and the extension on the cover becomes smaller.

In this study the vector is formed by the round-trip efficiency, power output, and efficiency of the discharge mode, which are relevant functions of the coupled system and are the only functions exhibiting convex behaviours. Introducing trade-off functions do not produce additional information in the optimization, since such compromises are already accounted in the Pareto front. Also, objectives from the HP subsystem such as ν and P_{in} will not be included because, as reported in a previous work [29], they exhibit monotonous behaviours. Only the efficiency of the HE-cycle, η, exhibits a maximum and its optimization could be of interest so these are the only functions that will be included in the optimization vector.

The algorithm described above is iterated until a well-defined Pareto front is obtained. This approach has 3 main stages (see the schematic diagram in Fig. 4). In the first stage the 18 parameters and the two a_c's are considered indistinctly as parameters/variables that enter into the algorithm. The corresponding allowed range of values are given in Table 2, both in an ideal non constrained configuration (second column in Table 2) as in the bounded configuration with restricted values for the parameters accounting for the internal irreversibilities (third column in Table 2).

From this first stage it is possible to determine that several parameters acquire the highest possible value that they are allowed to have and

Table 2

Range of interest for the 20 parameters. Ideal configurations are allowed in what is called the *free configuration*. Also, to check consistency, some parameters are bounded by upper values which are typical values in the literature (the bounded configuration). Tha range of possible values of each parameter is quite optimistic, but useful as a reference landmark. The values of a_c are determined by the physically acceptable region determined by the other 18 parameters.

Parameter	Free configuration	Bounded config.
$\epsilon_{c,t}^{HE,HP}$	$[0.9, 1]$	$[0.9, 0.95]$
$\rho_{H,L}^{HE,HP}$	$[0.97, 1]$	$[0.97, 0.99]$
$\epsilon_{H,L}^{HE,HP}$	$[0.9, 1]$	$[0.9, 0.95]$
$\Gamma_{H,L}^{HE,HP}$	$[0, 1]$	$[0, 1]$
$\xi^{HE,HP}$	$[0.01, 0.1]$	$[0.01, 0.1]$
$a_c^{HE,HP}$	$[1, 4]$	$[1, 4]$

Table 3

Irreversibilities defined from the parameters α and β.

Internal irrev.	$\alpha \in [0, 0.1]$	External irrev.	$\beta \in [0, 0.1]$
$\epsilon_{c,t} = 1 - \alpha$	$[1, 0.9]$	$\epsilon_{H,L} = 1 - \beta$	$[1, 0.9]$
$\rho_{H,L} = 1 - \frac{\alpha}{5}$	$[1, 0.98]$	$\xi = 0.01 + \frac{\beta}{2}$	$[0.01, 0.06]$

are not restricted by the physical constraints at hand. For robustness, this procedure is repeated to obtain 100 Pareto fronts in the free and the constrained configurations.

From the 20 parameters, those that could offer relevant information in the optimization process are only 5: $\{a_c^{HE}, a_c^{HP}, \Gamma_H^{HE}, \Gamma_L^{HE}, \Gamma_L^{HP}\}$. They will be used in the second stage. The rest of the parameters tend to the less irreversible configuration, as expected. Additionally, from this first stage it is obtained that the coefficient $\Gamma_H^{HP} \to 1$. Notice that $\Gamma_H^{HP} \to 0$ ($\Gamma_{H,L} \equiv \frac{C_w}{C_{H,L}}$) yields to constant temperature reservoirs (large reservoirs) leading to previously theoretical results, such as the so-called endoreversible limit [20,21,25]. By having $\Gamma_H^{HP} > 0$ the heat reservoirs will exhibit a variable temperature (finite size reservoirs). As it will be shown later, such cases allow for greater values of Φ compared with the case where the temperature of the thermal reservoirs are constant.

3.2. Determining an optimum design point

In a second stage, the 5-dimensional phase space is analysed. For visualization purposes first Φ and P_{out} are chosen as objective functions. For completeness the Pareto fronts from η and P_{out} (i.e. the optimization of the discharge mode) are shown in Appendix A.1 and the complete Pareto front for Φ, η and P_{out} is worked out in Appendix A.2.

To have certainty that the results stemming from this stage are consistent with a wide range of irreversibilities, a degree of irreversibility will be analysed through the parameters α and β, for internal and external irreversibilities, respectively (see definitions in Table 3). In this way, when $\alpha = \beta = 0$ there are no irreversibilities, and when $\alpha > 0$ and $\beta > 0$ the minimum efficiency of the compressor, turbine/expansor and exchangers will be of 90%, with maximum pressure drops of 6.8% for a monoatomic gas and 4.93% for a diatomic gas and maximum heat leaks of 6%. Although the values analysed here are quite optimistic, the constant improvement in the components efficiencies are considered, providing a long-lasting landmark.

In order to analyse the effect of increasing internal irreversibilities, β is first fixed in 3 representative values, $\{0, 0.05, 0.1\}$ (no external irreversibilities, a intermediate case and a more irreversible case) and in each case α takes the values $\{0, 0.01, 0.02, \ldots, 0.1\}$. The resulting Pareto front in the $\Phi - \bar{P}_{out}$ plane ($\bar{P}_{out} \equiv P_{out}/C_w$) is shown in Fig. 5a. Fig. 5b shows the corresponding outputs but in the $\eta - \bar{P}_{out}$ plane and Fig. 5c shows the Pareto optimal set in the $a_c^{HE} - a_c^{HP}$ space. A proper
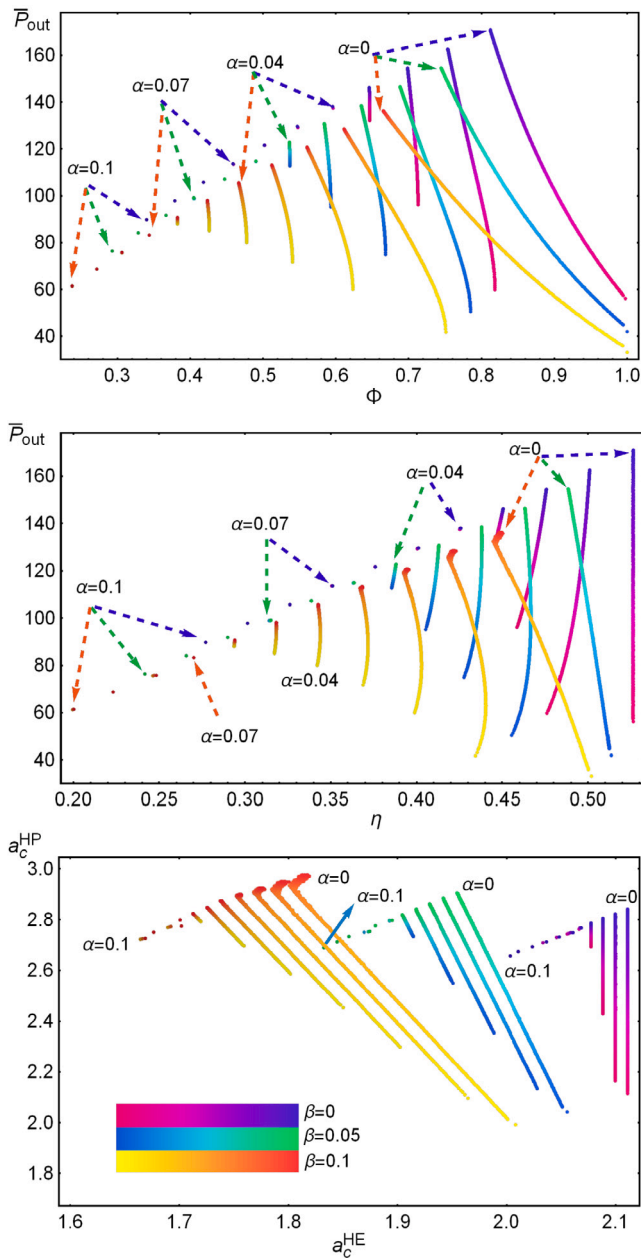
Fig. 6. Correspondence between the variable a_c and r_c for $\gamma = 5/3$ and $\gamma = 7/5$.

Fig. 5. Three cases of fixed external irreversibilities, $\beta = \{0, 0.05, 0.1\}$ with $\alpha = \{0, 0.01, 0.02, \ldots, 0.1\}$ (i.e. an step of 0.01 is taken). Different colour spectra differentiate each β case. In addition, for each β case the gradient is related with the normalized value of a_c^{HP} to keep track of its influence on the Pareto front. In (a) the Pareto front in the $\Phi - \bar{P}_{out}$; in (b) the corresponding points in the $\eta - \bar{P}_{out}$ plane; and in (c) the Pareto optimal set. The colour gradient allows for tracking the influence of a_c^{HP} in the Pareto front. (For interpretation of the references to colour in this figure legend, the reader is referred to the web version of this article.)

comparison of magnitudes for the involved pressure ratios is given in Fig. 6, where the correspondence between a_c and $r_c \equiv a_c^{\frac{\gamma}{\gamma-1}}$ (see Eqs. (6) and (7)).

Fig. 5a shows that, as expected, increasing the irreversibilities through β and α decreases both the maximum power output and round trip efficiency. Notice that only $\alpha = 0$ allows for $\Phi = 1$. Also note as the internal irreversibility factor α increases, the Pareto fronts exhibit a steeper negative slope. The optimization does not allow positive slopes, as it can be seen for large values of α (see last cases of β in Fig. 5a). In fact, at high enough α-values $\bar{P}_{out}$ and Φ collapse to a single point. These features apply to results in Fig. 5b. Concerning with the Pareto
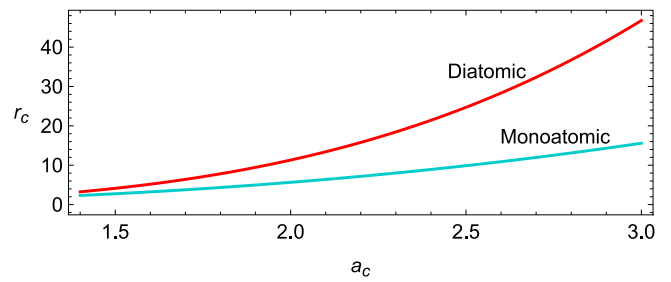
optimal set in Fig. 5c, clear evidences about the compression ratios are deduced: the gradient colour shows that large values of both a_c^P are related with maximum power states, meanwhile smaller values are related with maximum round-trip efficiency.

In Fig. 7 it is considered the case where α is fixed and β is allowed to vary in the considered interval. It offers new and valuable insights. In this case the relevance of internal irreversibilities is more evident. For large α the Pareto fronts are reduced to a single point in each case. Also, for medium values of α, there are no β values allowing $\Phi_{max} = 1$. Significant drops in both Φ and η are clearly visible. Note in particular the splitting of the Pareto front in well confined regions according to the relevance of the internal irreversibilities (none/medium/large): for each α case the set of β cases are disconnected. Thus, the dependence of the internal irreversibilities on the Pareto front (see Fig. 7b) is larger than that of the external ones. It is noteworthy that as the internal irreversibilities (α) increase (going from purple to blue to orange colours), the maximum values of a_c^{HP} decrease (see Fig. 7c).

After analysing all the resulting regions it is possible to determine an optimum configuration that requires the less mass flow difference between the reservoirs and the HE or the HP, that is, the larger possible value of each Γ that can be found in all the Pareto front. This allows to establish a design point. Recall that $\Gamma_{H,L} \equiv C_W/C_{H,L} = \frac{\dot{m}_w}{\dot{m}_{H,L}} \frac{c_{p\,w}}{c_{p\,H,L}}$, thus the ratio $\dot{m}_w/\dot{m}_{H,L}$ depend on the mass flow differences, this variable value of γ can be easily implemented with current technology. Some representative outcomes from the optimization are given in Fig. 8 for Γ_H^{HE}, Γ_L^{HE} and Γ_L^{HP}. The dashed horizontal lines indicate the largest Γ that gives access to all the Pareto front, larger values of a_c^{HE} are linked to maximum $\bar{P}_{out}$, meanwhile the leftmost a_c^{HE}'s to maximum Φ (see Figs. 5 and 7). Above this dashed lines an election of Γ could benefit from diminishing the reservoir mass flow and size but the system will not be able to perform in all regimes. Thus, relating achievable operation regimes with mass flows ratios between system and reservoirs. According to this criteria, the resulting configuration leads to the Γ's given in the first row of Table 4.

This whole procedure is repeated for the case where the optimization is focused only on the discharge subsystem (HE) by maximizing η and P_{out} (see Appendix A.1) and also for the case including the complete optimization through the three functions Φ, η and $\bar{P}_{out}$ (see Appendix A.2). The resulting ranges of Γ's for those cases are shown in the second and third rows of Table 4. By choosing the smallest Γ's appearing in Table 4 it is guaranteed the access to the whole spectrum of the Pareto front in all cases.

These values for the $\Gamma_{H,L}(\equiv \frac{C_w}{C_{H,L}})$ coefficients provide information of the system mass flow ratio. Interestingly this analysis shows that the best outcome is provided if all Γ's are the unity except for Γ_H^{HE}, which should be around $1/3$ of the rest of the Γ's. This is a relevant result (and not obvious *a priori*) stemming from the multiobjective and multiparametric optimization.
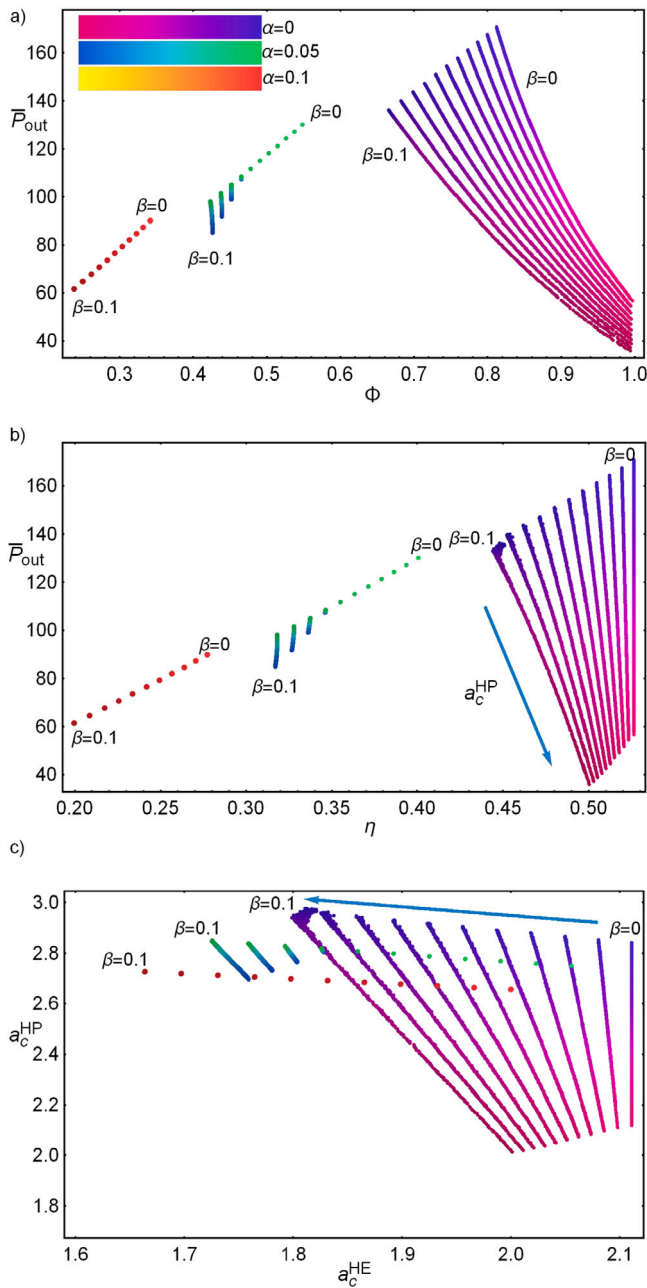
Fig. 7. Three cases of fixed internal irreversibilities, $\alpha = \{0, 0.05, 0.1\}$ with $\beta = \{0, 0.01, 0.02, \dots, 0.1\}$. In (a) the Pareto front, in (b) the corresponding points in the $\Phi - \bar{P}_{out}$ plane and in (c) the Pareto optimal set. The colour gradient allows for tracking the influence of a_c^{HP} in the Pareto front. (For interpretation of the references to colour in this figure legend, the reader is referred to the web version of this article.)

3.3. Multiobjective optimization in the design point

From the 5 parameters an optimal design has been provided through the Γ parameters with geometric and technological implications. A last step is the optimization involving only a_c^{HE} and a_c^{HP}. Internal and external irreversibilities will be analysed through the parameters α and β once again.

For this last optimization the influence of α and β is condensed to the case $\alpha = \beta$ and range from 0 to 0.1 with increments of 0.01. The resulting Pareto fronts are displayed in Fig. 9. For this last step, emphasis has been made in achieving the true Pareto front; for this
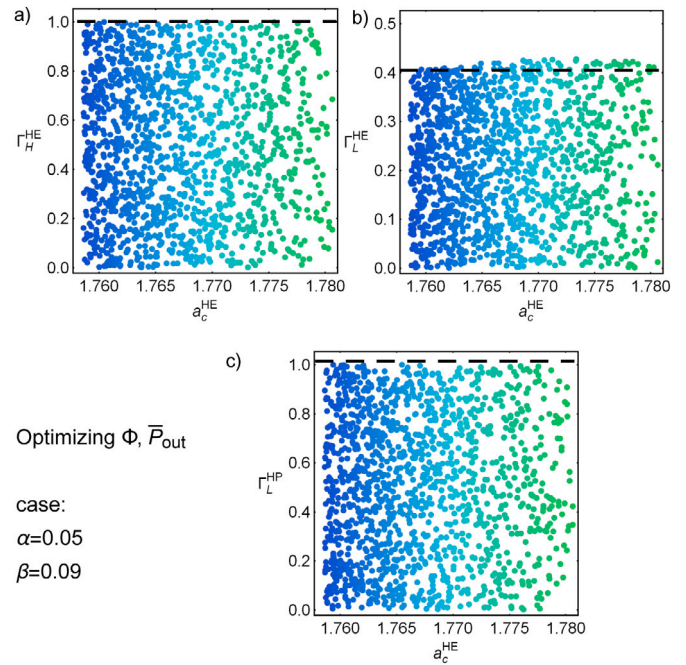

Fig. 8. Optimal set in a representative case with $\alpha = 0.05$ and $\beta = 0.09$. This is the typical behaviour exhibited after the optimization is made. It is of interest the largest Γ accessible from all the interval of a_c^{HE} (dashed horizontal lines), which provides access to all the optimum states. According to Figs. 5 and 7 the smallest a_c^{HE} produced the maximum available P_{out}, meanwhile the largest values produced the maximum available Φ. The colour scale correspond to the case $\alpha = 0.05$ in Fig. 7. (For interpretation of the references to colour in this figure legend, the reader is referred to the web version of this article.)

Table 4
The largest values of the $\Gamma_{H,L} \equiv C_W/C_{H,L}$ that give access to the whole Pareto front using Φ and $\bar{P}_{out}$ as objective functions, optimizing η and P_{out} (see Appendix A.1) and Φ, η and $\bar{P}_{out}$ (see Appendix A.2).

Optimum Γ_{HL} case $\Phi - P_{out}$			
Γ_H^{HE}	1	Γ_L^{HE}	0.4
Γ_H^{HP}	1	Γ_L^{HP}	1
Optimum Γ_{HL} case $\eta - P_{out}$			
Γ_H^{HE}	1	Γ_L^{HE}	0.35
Γ_H^{HP}	1	Γ_L^{HP}	1
Optimum Γ_{HL} case $\Phi - P_{out} - \eta$			
Γ_H^{HE}	1	Γ_L^{HE}	0.35
Γ_H^{HP}	1	Γ_L^{HP}	1

reason the convergence to it has been quantified through the Kullback–Leibler divergence [34] between the probability distributions of Φ in every iteration of the algorithm introduced in Section 3.1 (see Appendix B).

Two relevant stripes can be seen by analysing the behaviour of Φ in Fig. 9. The transition from $\alpha = \beta = 0.03$ to 0.04 is crucial as the round-trip efficiency is largely affected in this irreversibility zone with upper values dropping from $\Phi_{max} = 1$ to 0.6 (see Fig. 9b) and from $\alpha = \beta = 0.04$ there is no difference between optimizing the power output and the round-trip efficiency. The representation of these Pareto fronts in the $\Phi - \bar{P}_{out}$ plane and in the $\phi - \eta - \bar{P}_{out}$ space are given in Fig. 9b–d.

To give an idea of the kind of configurations that could be expected coming from this optimization, three representative cycles for the particular configuration $\alpha = \beta = 0.01$ are shown in Fig. 10.
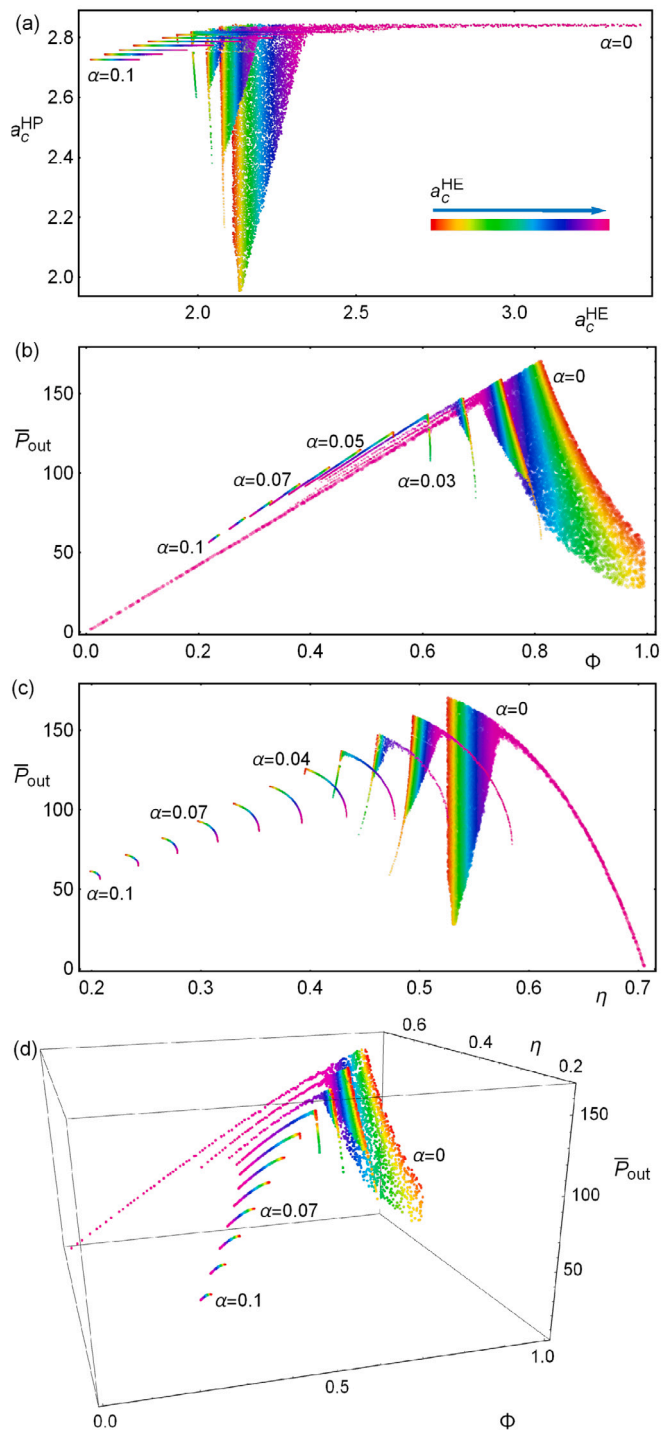
Fig. 9. Multiobjective optimization in the so-called optimal design configuration. The functions of interest are η, P_{out} and Φ. Internal and external irreversibilities vary as $\alpha = \{0, 0.01, 0.02, \dots, 0.1\}$. The colour gradient varies according to the normalized value of a_c^{HE}, which allows for tracking its influence in the Pareto front. In this way, red indicates low values of a_c^{HE} which corresponds to lower efficiency and better behaviour in both power output and round-trip efficiency, while the magenta colour corresponds to large a_c^{HE}'s and large efficiencies. In (a) the Pareto optimal set in the $a_c^{HE,HP}$ space. In (b)–(c) the Pareto front in the $\bar{P}_{out} - \Phi$ and the $\eta - \bar{P}_{out}$ planes, respectively. In (d) the corresponding Pareto front in the $\eta - \bar{P}_{out} - \Phi$ space. (For interpretation of the references to colour in this figure legend, the reader is referred to the web version of this article.)

For this, the working fluid is considered as a monatomic ideal gas and the storage reservoir is solar salt and the cryogenic substance is anhydrous methanol. This choice of reservoirs limits the temperatures

Table 5

Maximum achievable Φ as the internal and external irreversibilities increase with the parameters α and β, respectively. Green colour denotes best performance which degrades with a transition to yellow colours. Orange colours apply for the worst scenario.

$\alpha \backslash \beta$	0	0.01	0.02	0.03	0.04	0.05	0.06	0.07	0.08	0.09	0.1
0	1	1	1	1	1	1	1	1	1	1	1
0.01	0.82	0.81	0.8	0.8	0.79	0.78	0.78	0.77	0.76	0.76	0.75
0.02	0.71	0.7	0.69	0.69	0.68	0.67	0.66	0.65	0.64	0.63	0.62
0.03	0.65	0.63	0.62	0.61	0.6	0.59	0.58	0.57	0.56	0.55	0.54
0.04	0.6	0.58	0.57	0.56	0.55	0.54	0.52	0.51	0.5	0.49	0.48
0.05	0.55	0.54	0.53	0.51	0.5	0.49	0.48	0.46	0.45	0.44	0.43
0.06	0.5	0.49	0.48	0.47	0.46	0.45	0.43	0.42	0.41	0.4	0.38
0.07	0.46	0.45	0.44	0.43	0.42	0.4	0.39	0.38	0.37	0.36	0.34
0.08	0.42	0.41	0.4	0.39	0.38	0.37	0.35	0.34	0.33	0.32	0.31
0.09	0.38	0.37	0.36	0.35	0.34	0.33	0.32	0.31	0.29	0.28	0.27
0.1	0.34	0.33	0.32	0.31	0.3	0.29	0.28	0.27	0.26	0.25	0.24

Table 6

Maximum achievable η as the internal and external irreversibilities increase with the parameters α and β, respectively. Colour meanings as in previous table.

$\alpha \backslash \beta$	0	0.01	0.02	0.03	0.04	0.05	0.06	0.07	0.08	0.09	0.1
0	0.71	0.71	0.70	0.70	0.70	0.70	0.70	0.70	0.70	0.70	0.70
0.01	0.59	0.58	0.58	0.58	0.58	0.57	0.57	0.57	0.57	0.56	0.56
0.02	0.53	0.53	0.53	0.52	0.52	0.52	0.51	0.51	0.51	0.50	0.50
0.03	0.49	0.48	0.48	0.48	0.47	0.47	0.47	0.46	0.46	0.45	0.45
0.04	0.45	0.45	0.44	0.44	0.43	0.43	0.42	0.42	0.42	0.41	0.41
0.05	0.42	0.41	0.41	0.40	0.40	0.39	0.39	0.38	0.38	0.37	0.37
0.06	0.38	0.38	0.37	0.37	0.36	0.36	0.35	0.35	0.34	0.34	0.33
0.07	0.36	0.35	0.34	0.34	0.33	0.33	0.32	0.32	0.31	0.30	0.30
0.08	0.33	0.32	0.32	0.31	0.30	0.30	0.29	0.28	0.28	0.27	0.27
0.09	0.30	0.30	0.29	0.28	0.28	0.27	0.26	0.26	0.25	0.24	0.24
0.1	0.28	0.27	0.26	0.26	0.25	0.24	0.24	0.23	0.22	0.21	0.21

of the cryogenic reservoir to the range of $\left[175 \text{ K}, 337.5 \text{ K}\right]$ and the solar salt should be maintained in the range of $\left[511 \text{ K}, 858 \text{ K}\right]$ (see Table 1). In Fig. 10a the optimal set is represented in the r_c space and from this set three particular cases are depicted: in Fig. 10b that of η_{max}, in Fig. 10c that of Φ_{max} and in Fig. 10d that corresponding to $\bar{P}_{out,max}$. The three $T - S$ planes have the same scale to compare the geometrical differences among the three cases. The main differences between these results and the theoretical ones, see Fig. 11 in [29] are the larger values of the entropy and small values of temperature at the salt tanks in the case of maximum round-trip efficiency. For maximum efficiency the area of the HP is noticeably larger than that of the HE, meaning that Φ is small, which can be seen from Fig. 9d, the larger η the lesser Φ.

4. Maximum values of Φ, P_{out} and η

Tables 5, 6, and 7 show the maximum values that can be obtained for the round-trip efficiency, the HE efficiency, and the power output, respectively, as the irreversible parameters increase starting from the totally reversible case in the so-called optimum configuration. As it can be seen in Table 5 only the case of no internal irreversibilities allow for $\Phi = 1$. Notice that the influence of the external irreversibilities is more relevant as it is seen by comparing the drops in each column and in each raw, leading from $\Phi = 1$ down to 0.24 in the worst case. This is also the case for the maximum efficiency (Table 6), where the effect of internal irreversibilities is marginal, even for large irreversibilities. Also for the maximum power output (Table 7) the influence of external irreversibilities is larger than the internal irreversibilities.

In Table 4 the optimized values of the corresponding $\Gamma_{H,L}^{HE,HP}$ were detailed. For completeness, the two extreme cases of $\Gamma_{H,L}^{HE} \to 1$ and
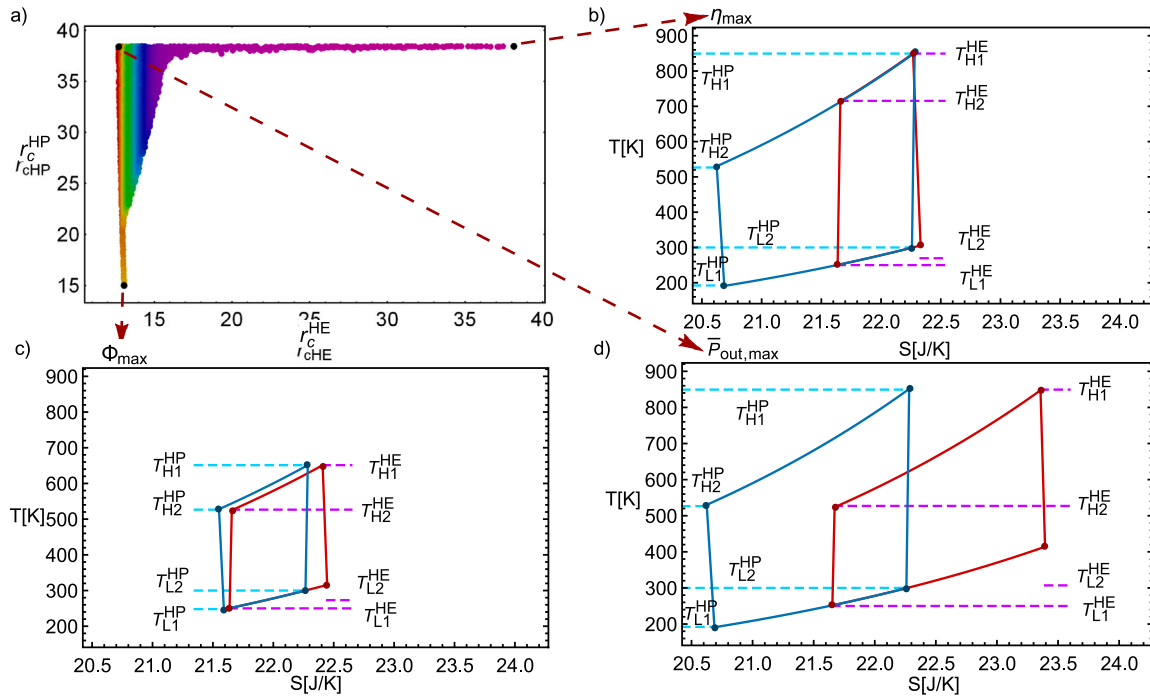
Fig. 10. (a) Pareto optimal set when optimizing Φ, P and η. The colour scale correspond to the values of a_c^{HE}, as mentioned in Fig. 9: red indicates low values of a_c^{HE} which are related to lower efficiency and better behaviour in both power output and round-trip efficiency, while the magenta colour corresponds to large a_c^{HE}'s and large efficiencies. Three representative layouts of the coupled PTES in the temperature–entropy space from the Pareto optimal set with $\alpha = \beta = 0.01$. These three layouts correspond to: (b) $\eta_{max} = 0.58$; (c) $\Phi_{max} = 0.81$; and (d) $\bar{P}_{out,max}/C_w = 159$ K. (For interpretation of the references to colour in this figure legend, the reader is referred to the web version of this article.)

Table 7
Maximum achievable $\bar{P}_{out} \equiv P_{out}/C_w$ as the internal and external irreversibilities increase with the parameters α and β, respectively. Colour meanings as in previous table.

| $\alpha \setminus \beta$	0	0.01	0.02	0.03	0.04	0.05	0.06	0.07	0.08	0.09	0.1
0	171	168	164	161	158	154	151	147	144	140	136
0.01	162	159	156	153	150	146	143	139	136	132	128
0.02	154	151	148	145	142	138	135	132	128	124	120
0.03	146	143	140	137	134	130	127	124	120	117	113
0.04	138	135	132	129	126	123	119	116	112	109	105
0.05	130	127	124	121	118	115	112	108	105	101	98
0.06	122	119	116	113	110	107	104	101	97	94	90
0.07	114	111	108	105	102	99	96	93	90	86	83
0.08	106	103	100	97	95	92	89	85	82	79	76
0.09	98	95	92	90	87	84	81	78	75	72	68
0.1	90	87	85	82	79	76	73	70	67	64	61

Table 8
Φ at MP conditions. Green colour denotes performances around the endoreversible case, which corresponds to the value $\Phi_{MP,endo} = 0.57$, as the colour goes blue Φ present larger values, and as the colour tend to yellow, lower values.

$\alpha \setminus \beta$	0	0.01	0.02	0.03	0.04	0.05	0.06	0.07	0.08	0.09	0.1
0	0.81	0.8	0.78	0.77	0.76	0.74	0.73	0.71	0.7	0.68	0.66
0.01	0.75	0.74	0.73	0.71	0.7	0.69	0.67	0.66	0.64	0.63	0.61
0.02	0.7	0.69	0.67	0.66	0.65	0.63	0.62	0.61	0.59	0.57	0.56
0.03	0.64	0.63	0.62	0.61	0.6	0.58	0.57	0.56	0.54	0.53	0.51
0.04	0.6	0.58	0.57	0.56	0.55	0.54	0.52	0.51	0.49	0.48	0.47
0.05	0.55	0.54	0.53	0.51	0.5	0.49	0.48	0.46	0.45	0.44	0.42
0.06	0.5	0.49	0.48	0.47	0.46	0.45	0.43	0.42	0.41	0.4	0.38
0.07	0.46	0.45	0.44	0.43	0.42	0.4	0.39	0.38	0.37	0.36	0.34
0.08	0.42	0.41	0.4	0.39	0.38	0.37	0.35	0.34	0.33	0.32	0.31
0.09	0.38	0.37	0.36	0.35	0.34	0.33	0.32	0.31	0.29	0.28	0.27
0.1	0.34	0.33	0.32	0.31	0.3	0.29	0.28	0.27	0.26	0.25	0.24

$\Gamma_{H,L}^{HE} \to 0$ have been also analysed and the corresponding results are collected in Appendix C for $\bar{P}_{out,max}$, η_{max} and Φ_{max}. The case of $\Gamma_{H,L}^{HE} \to 1$ (or finite reservoirs with $C_{H,L} \to C_w$) is presented in Table C.9. Most noticeable is that the range of the parameter α accounting for internal irreversibilities is strongly reduced as the Pareto results delimit its value up to $\alpha = 0.7$. As a consequence the performance values of $\bar{P}_{out,max}$, η_{max} and Φ_{max} strongly decrease getting lower values even for small values of external irreversibilities. The results for $\Gamma \to 0$ (or reservoirs with $C_{H,L} \to \infty$) are presented in Table C.10. It is evident that also this limit case is not successful, specially in the values presented by the power output which diminishes its value as the internal and external irreversibilities increase. Similar trends are displayed by the maximum efficiency and maximum round trip efficiency. Thus, the present analysis has shown the benefits of including the geometric-design parameters into the optimization, with no obvious consequences.

5. Φ at maximum power: endoreversible limit

In the literature it has been reported the case of theoretical models with infinite heat reservoirs at constant temperature using Carnot-like arrangements where only external irreversibilities are taken into account due to the coupling of the (reversible) inner cycle to the external reservoirs. In this last case, the so-called endoreversible limit (i.e., no internal irreversibilities) has been analysed. The reported round-trip efficiency under maximum power conditions has a dependence only of the extreme external temperatures ratio $\tau < 1$, with a value of $\Phi_{MP} = \frac{2-\sqrt{\tau}}{2+\sqrt{\tau}}$. It is noteworthy that the present model is able to reproduce the results for the endoreversible case [20,21] under some assumptions:
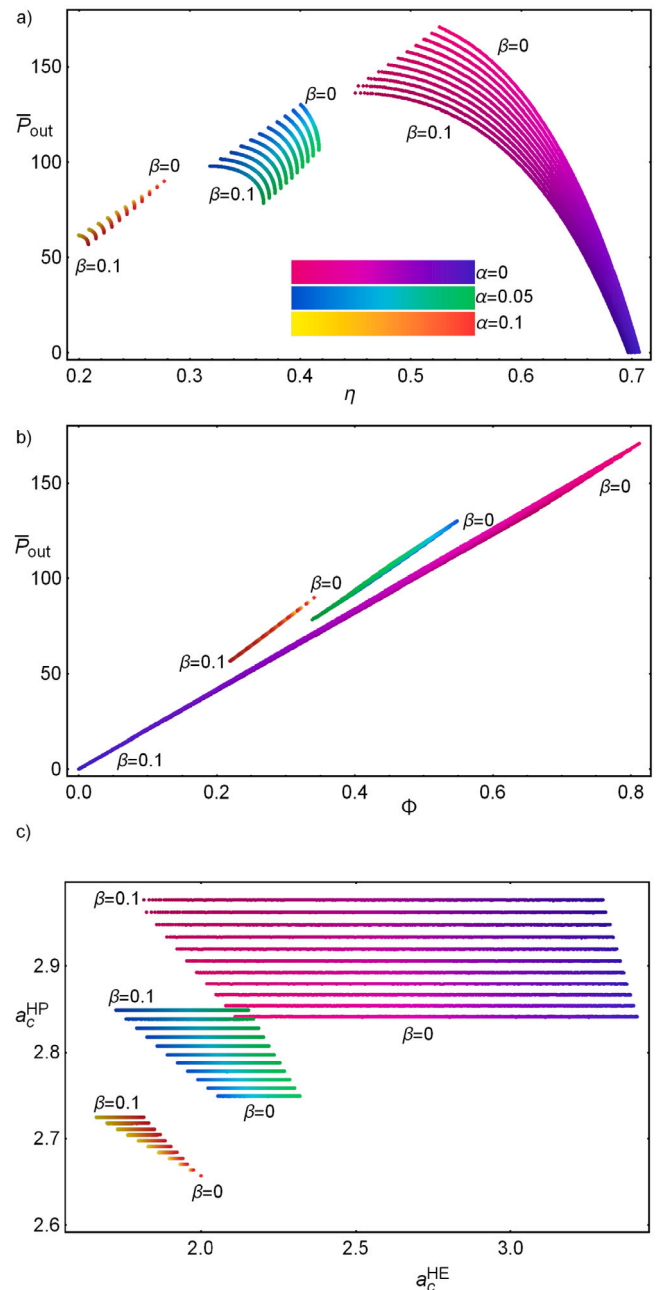
- Internal irreversibilities are zero ($\rho = 1$, $\epsilon_{t,c} = 1$).
- The Q_h pumped to the storage reservoir is completely transmitted to the discharge mode. This fact constraints a_c^{HP}.
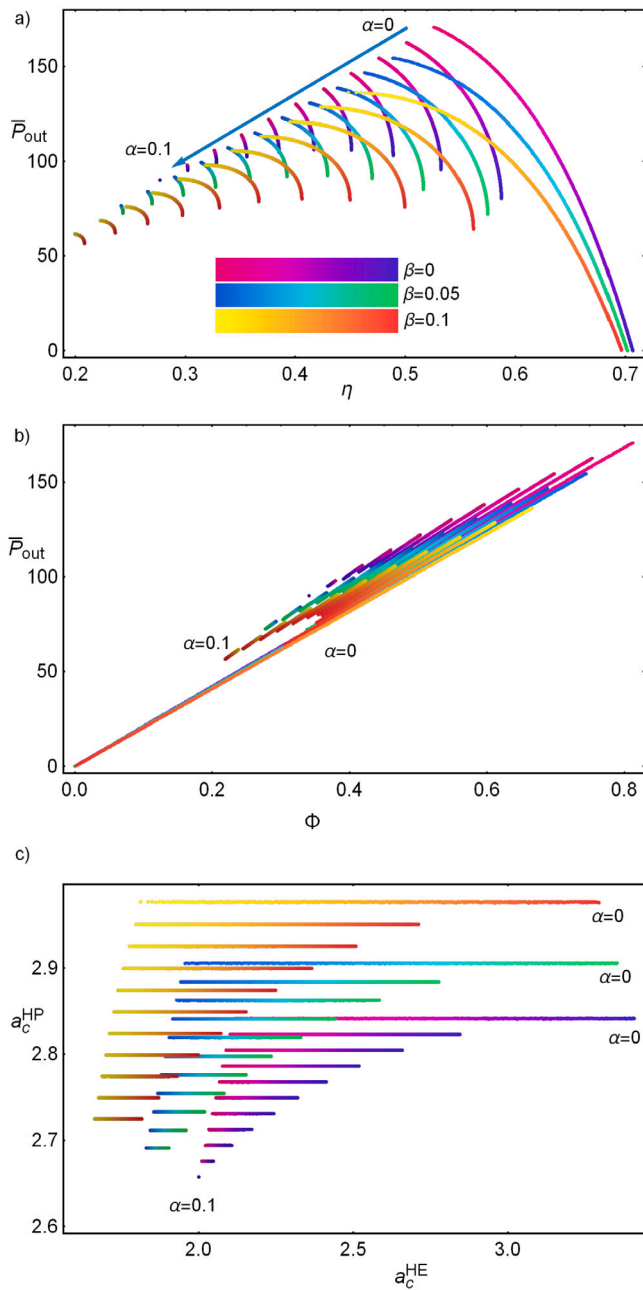
Fig. A.11. Optimization of the HE through η and $\bar{P}_{out}$ as the objective functions. Three cases of fixed external irreversibilities, $\beta = \{0, 0.05, 0.07\}$ with internal irreversibilities: $\alpha = \{0, 0.01, 0.02, \ldots, 0.1\}$. Different colour spectra differentiate each β case. In addition, for each β case the gradient is related with the normalized value of a_c^{HE} to keep track of its influence on the Pareto front. In (a) the Pareto front, in (b) the corresponding points in the $\Phi - \bar{P}_{out}$ plane and in (c) the Pareto optimal set. The colour gradient allows for tracking the influence of a_c^{HE} in the Pareto front. (For interpretation of the references to colour in this figure legend, the reader is referred to the web version of this article.)

Fig. A.12. Optimization of the HE through η and $\bar{P}_{out}$ as the objective functions. Three cases of fixed internal irreversibilities, $\alpha = \{0, 0.05, 0.07\}$ with external irreversibilities: $\beta = \{0, 0.01, 0.02, \ldots, 0.1\}$. In (a) the Pareto front, in (b) the corresponding points in the $\Phi - \bar{P}_{out}$ plane and in (c) the Pareto optimal set. The colour gradient allows for tracking the influence of a_c^{HE} in the Pareto front. (For interpretation of the references to colour in this figure legend, the reader is referred to the web version of this article.)

- All stored heat is used in the discharge and, then, there is no heat leak.
- $\tau = T_L^{HE}/T_H^{HE} = T_L^{HP}/T_H^{HP}$ (compare with the case in Fig. 10).

For that case $a_c^{HE} = \sqrt{\tau^{-1}}$, $a_c^{HP} = (2 - \sqrt{\tau})/\tau$ and $\Phi_{MP} = \frac{2-\sqrt{\tau}}{2+\sqrt{\tau}}$, which is the same than those previously reported. For the representative case of Solar Salt, with Anhydrous Methanol and by choosing $T_L = 250$ K and $T_H = 850$ K it is obtained $\tau = 0.29$ and $\Phi_{MP} = 0.57$. To have an estimate of how distant is this result from the cases stemming

from the present analysis Table 8 shows the values of Φ_{MP} in the optimum design point ($\Gamma_{H,L}^{HP} = \Gamma_H^{HE} = 1$ and $\Gamma_L^{HP=0.35}$) and considering internal and external irreversibilities. Notice that despite the presence of irreversibilities, there is a wide range of them that still produce round-trip efficiencies larger than that of the endoreversible case. Also notice in Table 8 that the heat leak is never zero, according to Table 2 the minimum heat leak is $\xi = 0.01$.

6. Summary and conclusions

A multiparametric and multiobjective optimization of a combined PTES system for energy storage in liquid media based on Brayton-like
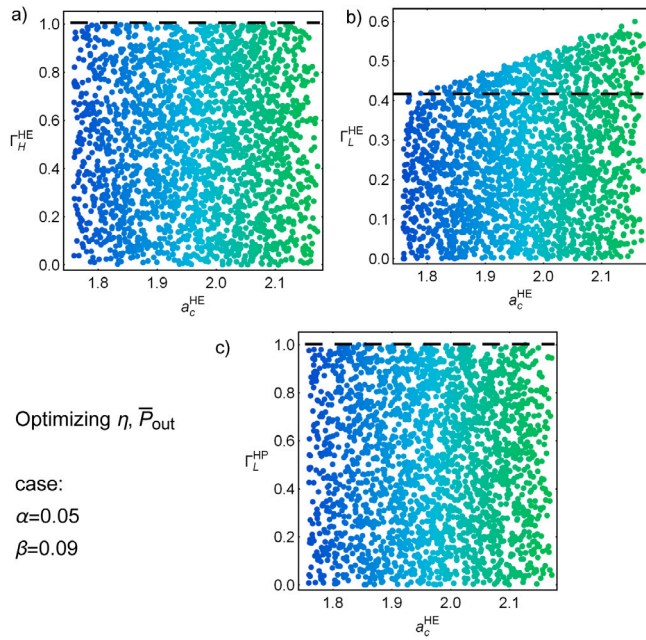
Fig. A.13. Optimal set in a representative case with $\alpha = 0.05$ and $\beta = 0.09$. This is the typical behaviour exhibited after the optimization is made. It is of interest the largest Γ accessible from all the interval of a_c^{HE}, which provides access to all the optimum states. According to Figs. 5 and 7 the smallest a_c^{HE} produced the maximum available $\bar{P}_{out}$, meanwhile the largest values produced the maximum available Φ.

Fig. A.14. The best compromise among Φ, η and $\bar{P}_{out}$. Above: Three cases of fixed external irreversibilities, $\beta = \{0, 0.05, 0.07\}$ with internal irreversibilities: $\alpha = \{0, 0.01, 0.02, \ldots, 0.1\}$. Below: Three cases of fixed internal irreversibilities, $\alpha = \{0, 0.05, 0.07\}$ with external irreversibilities: $\beta = \{0, 0.01, 0.02, \ldots, 0.1\}$. The colour gradient allows for tracking the influence of a_c^{HE} in the Pareto front. (For interpretation of the references to colour in this figure legend, the reader is referred to the web version of this article.)

cycles has been addressed by the calculations of different Pareto fronts. The main objectives have been to analyse the role of the internal and external irreversibilities as well as the mass flow ratios between the working fluid and the reservoirs and to obtain the best performance including the round-trip efficiency, power output, and efficiency as objective functions. The optimization has been developed in three stages: (a) using all the available parameters; (b) determining an optimal design point with five parameters; and (c) a final optimization through the compression ratios. In each case, explicit results have been obtained under maximum round trip efficiency and power output conditions, under maximum power and maximum efficiency conditions and under maximum round-trip efficiency, power and efficiency conditions.

From (a) it was obtained that the ratio between the heat capacities of the working fluid in the HP and the cold reservoir should be the same ($C_W^{HP}/C_L = 1$, less size difference and similar mass flow). No constraints on the irreversibilities were found.

From (b) The optimization revealed a preference for having the same heat capacity in the working fluid and the hot reservoirs, $C_W/C_H = 1$ as in the case of the cold reservoir, but $C_W^{HE}/C_L = 0.35$, constraining the size and the mass flow in the case of the HE. This constraint is used to propose a design point.

From (c) it was shown that the performance in the optimum design point can increase substantially the energetic performance of the PTES, up to 49% for the round-trip efficiency over the endoreversible case under maximum power conditions (see Table 8).

The size and the mass flow of the TES media is an important parameter from economic and technical points of view. The present multiparametric optimization shows a non-trivial outcome as to what scale factor among the working fluid heat capacity and those of the TES's provides with the best benefit for the desired objective functions.

As can be seen from the obtained configurations the final temperatures T_{H2}^{HP} and T_{H2}^{HE} are different, this in fact would require an stabilization mechanism in the transition between charge and discharge processes. To recover a heat rejection for a continuous operation, the
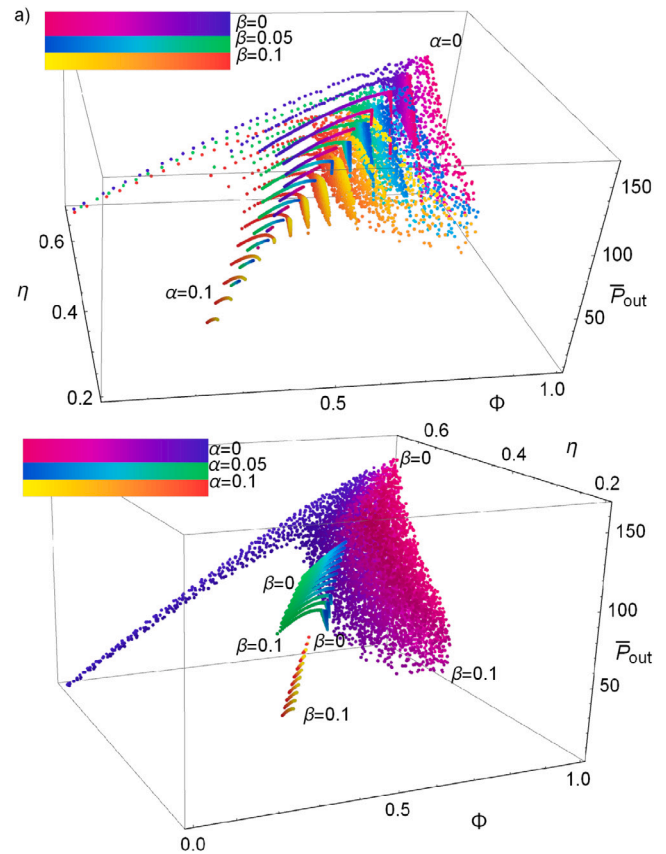
stabilization and the coupling with other subsystem are still pending jobs for future research.

CRediT authorship contribution statement

J. Gonzalez-Ayala: Conceptualization, Writing – original draft, Software, Validation, Formal analysis, Writing – review & editing. **D. Salomone-González:** Writing – original draft, Validation, Formal analysis, Writing – review & editing. **A. Medina:** Conceptualization, Supervision, Writing – original draft, Validation, Formal analysis, Writing – review & editing. **J.M.M. Roco:** Supervision, Writing – original draft, Validation, Formal analysis, Writing – review & editing. **P.L. Curto-Risso:** Supervision, Writing – original draft, Validation, Formal analysis, Writing – review & editing, Funding acquisition. **A. Calvo Hernández:** Conceptualization, Supervision, Writing – original draft, Validation, Formal analysis, Writing – review & editing.
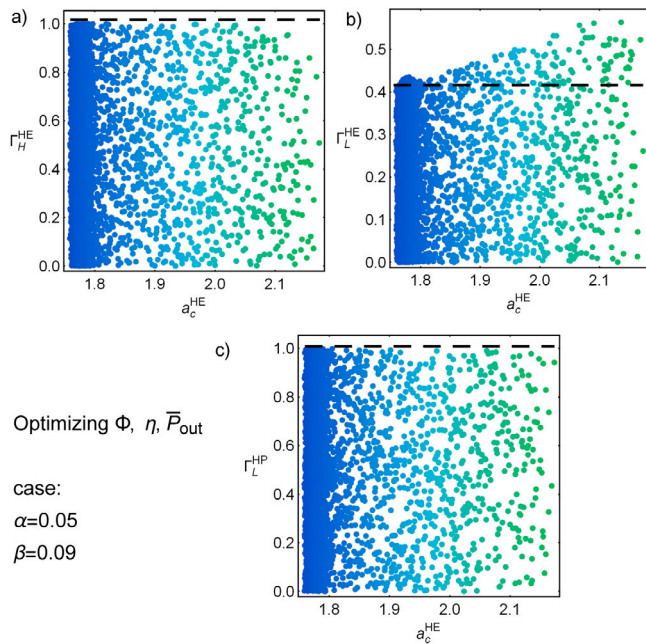
Acknowledgements

Fig. A.15. Optimal set in a representative case with $\alpha = 0.05$ and $\beta = 0.09$. This is the typical behaviour exhibited after the optimization is made. It is of interest the largest Γ accessible from all the interval of a_c^{HE}, which provides access to all the optimum states. According to Figs. 5 and 7 the smallest a_c^{HE} produced the maximum available $\bar{P}_{out}$, meanwhile the largest values produced the maximum available Φ.

Appendix A. Multiobjective optimization: selection of design point

By realizing the optimization of three different cases of objective functions: $\Phi - \bar{P}_{out}$ ($\bar{P}_{out} \equiv P_{out}/C_w$) for the overall PTES system (addressed in Section 3.2), $\eta - \bar{P}_{out}$ for the discharge subsystem and $\Phi - \eta - \bar{P}_{out}$ for the combination of the charge and the discharge systems, it is possible to define regions of interest from where to chose the best

values for $\Gamma_{H,L}^{HE,HP}$. The proper choice of the Γ's will have repercussions in the scale of the HP-HE and thermal reservoirs (TES). As discussed in the concluding remarks this is one of the key outcomes of the paper.

A.1. Pareto front using η and P_{out} as objective functions

In the same way that the Pareto front was obtained using the global functions for the PTES, Φ and $\bar{P}_{out}$, now the result of optimizing only the HE subsystem is presented, i.e., the objective functions to be considered are η and $\bar{P}_{out}$. The analysis is parallel to that presented in Section 3.2. The results can be seen in Fig. A.11 for fixed β and increasing the internal irreversibilities and in Fig. A.12 for three cases where α is fixed and the external irreversibilities are increased.

The resulting optimal set is mapped to the energetic space Φ, η and $\bar{P}_{out}$. In all cases they are monotonic functions of a_c^{HE}. Naturally, if the HE subsystem is the one being optimized, it is expected that this variable is the one determining the optimum states. Notice that the three cases of fixed external irreversibilities (Fig. A.12) produce similar Pareto fronts. On the other hand, those at constant internal irreversibility are located in quite different regions, showing once again that the sensibility regarding the internal irreversibilities is significant.

It is remarkable that as the internal irreversibilities increase, a_c^{HP} is constraint to smaller values. In the case of the Γ's there are valuable information that can be obtained by considering all the combinations of irreversibilities. As can be seen in Figs. 5 and 7, Φ, η and $\bar{P}_{out}$ are monotonic functions of a_c^{HE}, thus, values of Γ that allow the obtaining of such maximum states are of interest. In Fig. A.13 some representative outcomes from the optimization are depicted. In each case the value of interest is the largest Γ that is accessible at all a_c^{HE}'s. The infimum of all these values will determine the best Γ, assuming that it is interest to have the smallest possible reservoirs and allowing all possible operation regimes at the same time.

A.2. Pareto front using Φ, η and P_{out} as objective functions

The same multiobjective and multiparametric procedure to optimization by using the three objective functions that exhibit convex behaviours Φ, η and $\bar{P}_{out}$. The results are displayed in Fig. A.14. In Fig. A.15 some representative outcomes from the $\Phi - \eta - \bar{P}_{out}$ optimization are depicted.
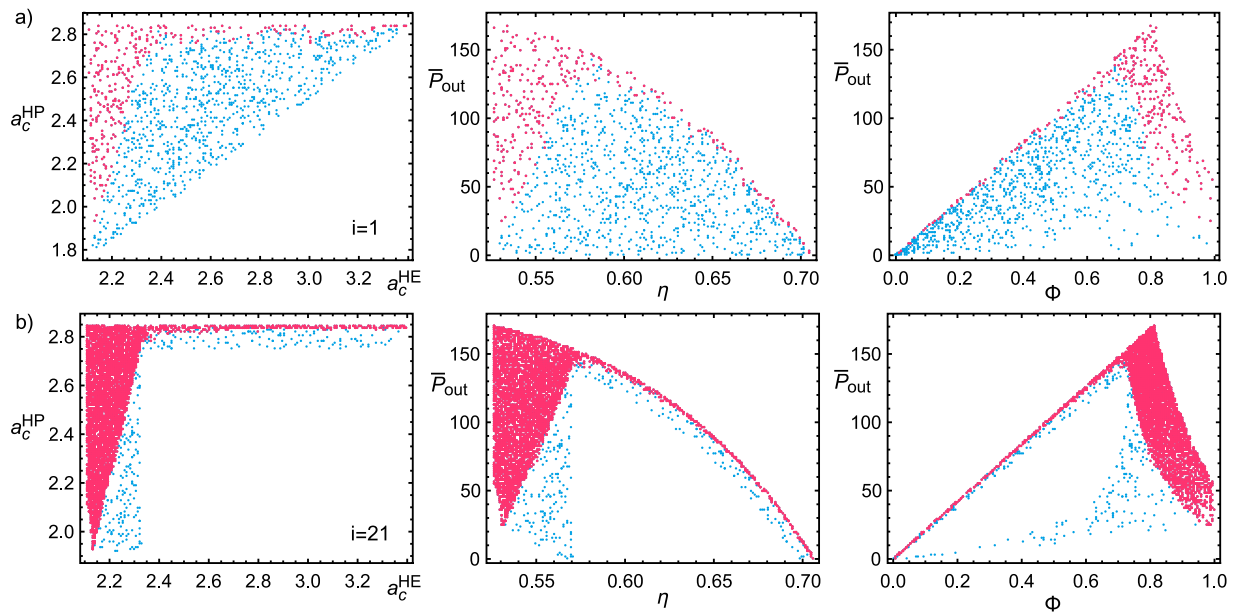

Fig. B.16. Two representative search steps in the optimization algorithm described in Section 3.1 once the optimum PTES configuration has been determined. In (a) the first step of the random search in the physically acceptable region. These points in the phase space are mapped in the $\eta - P_{out}$ and in the $\Phi - \bar{P}_{out}$ planes. In (b) the step 21 in the iteration of the search algorithm.
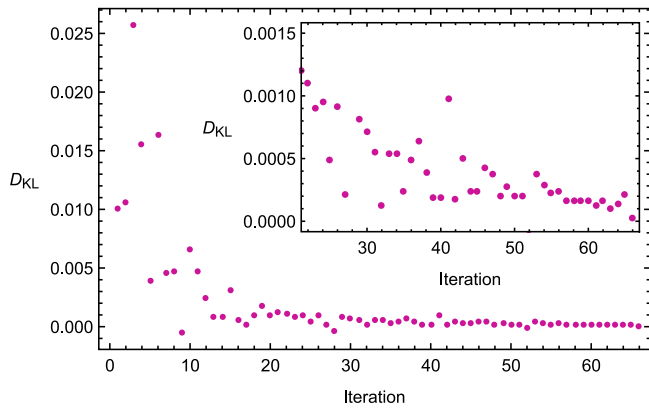
Fig. B.16. A representative case of the evolution of the D_{KL} for the case $\alpha = \beta = 0.07$ and searching for 400 random points in each iteration. From the 20th iteration it can be seen that D_{KL} has a stable decreasing behaviour. At iteration 66 the threshold is achieved, producing a Pareto front of 15 822 points.

Table C.9

Maximum achievable values of Φ, η, $\bar{P}_{out} \equiv P_{out}/C_w$ as the internal and external irreversibilities increase with the parameters α and β, respectively when all $\Gamma \to 1$. Notice that the maximum value allowed for α is 0.07. Green colour denotes best performance which degrades going progressively to yellow colours and red colours for the worst scenario.

| Φ_{max} | | | | | | | | | | | |
$\alpha \setminus \beta$	0	0.01	0.02	0.03	0.04	0.05	0.06	0.07	0.08	0.09	0.1
0	1	1	1	1	1	1	1	1	1	1	1
0.01	0.82	0.81	0.80	0.80	0.79	0.78	0.78	0.77	0.76	0.76	0.75
0.02	0.70	0.69	0.69	0.68	0.67	0.66	0.66	0.65	0.64	0.63	0.62
0.03	0.59	0.58	0.57	0.57	0.56	0.55	0.55	0.54	0.53	0.52	0.52
0.04	0.47	0.46	0.45	0.45	0.44	0.44	0.43	0.42	0.42	0.41	0.40
0.05	0.34	0.34	0.33	0.33	0.32	0.32	0.31	0.31	0.30	0.30	0.29
0.06	0.21	0.21	0.21	0.20	0.20	0.20	0.19	0.19	0.19	0.18	0.18
0.07	0.09	0.08	0.08	0.08	0.08	0.07	0.07	0.07	0.07	0.07	0.06

| η_{max} | | | | | | | | | | | |
$\alpha \setminus \beta$	0	0.01	0.02	0.03	0.04	0.05	0.06	0.07	0.08	0.09	0.1
0	0.71	0.71	0.70	0.70	0.70	0.70	0.70	0.70	0.70	0.70	0.70
0.01	0.59	0.58	0.58	0.58	0.58	0.57	0.57	0.57	0.57	0.56	0.56
0.02	0.53	0.53	0.53	0.52	0.52	0.52	0.51	0.51	0.51	0.50	0.50
0.03	0.48	0.48	0.47	0.47	0.47	0.46	0.46	0.46	0.45	0.45	0.45
0.04	0.41	0.40	0.40	0.40	0.40	0.39	0.39	0.39	0.38	0.38	0.38
0.05	0.30	0.30	0.30	0.30	0.29	0.29	0.29	0.29	0.29	0.28	0.28
0.06	0.18	0.18	0.18	0.18	0.18	0.17	0.17	0.17	0.17	0.16	0.16
0.07	0.08	0.08	0.07	0.07	0.07	0.07	0.07	0.06	0.06	0.06	0.06

| $\bar{P}_{out,max}$ | | | | | | | | | | | |
$\alpha \setminus \beta$	0	0.01	0.02	0.03	0.04	0.05	0.06	0.07	0.08	0.09	0.1
0	131	129	128	126	124	122	120	118	117	115	113
0.01	114	113	111	110	108	107	105	104	102	101	99
0.02	97	96	94	93	92	91	89	88	87	85	84
0.03	78	77	76	75	74	73	72	71	70	69	68
0.04	58	57	57	56	56	55	54	53	53	52	51
0.05	37	37	36	36	36	35	35	34	34	34	33
0.06	19	19	19	18	18	18	17	17	17	17	16
0.07	7	7	7	7	6	6	6	6	6	5	5

Table C.10

Maximum achievable values of Φ, η, $\bar{P}_{out}$ as the internal and external irreversibilities increase with the parameters α and β, respectively when the TES temperatures are constant ($\Gamma \to 0$). Green colour denotes best performance which degrades going progressively to yellow colours and red colours for the worst scenario.

| Φ_{max} | | | | | | | | | | | |
$\alpha \setminus \beta$	0	0.01	0.02	0.03	0.04	0.05	0.06	0.07	0.08	0.09	0.1
0	1	1	1	1	1	1	1	1	1	1	1
0.01	0.67	0.67	0.67	0.66	0.66	0.65	0.65	0.64	0.63	0.63	0.62
0.02	0.52	0.51	0.50	0.50	0.49	0.49	0.48	0.47	0.47	0.46	0.46
0.03	0.41	0.41	0.40	0.39	0.39	0.38	0.37	0.37	0.36	0.35	0.35
0.04	0.33	0.33	0.32	0.31	0.31	0.30	0.29	0.28	0.28	0.27	0.26
0.05	0.27	0.26	0.26	0.25	0.24	0.24	0.23	0.22	0.21	0.21	0.20
0.06	0.22	0.21	0.20	0.20	0.19	0.18	0.18	0.17	0.16	0.15	0.15
0.07	0.17	0.17	0.16	0.15	0.15	0.14	0.13	0.12	0.12	0.11	0.10
0.08	0.14	0.13	0.12	0.11	0.11	0.10	0.09	0.09	0.08	0.07	0.07
0.09	0.10	0.10	0.09	0.08	0.07	0.07	0.06	0.05	0.05	0.04	0.03
0.1	0.07	0.07	0.06	0.05	0.05	0.04	0.03	0.03	0.02	0.01	0.01

| η_{max} | | | | | | | | | | | |
$\alpha \setminus \beta$	0	0.01	0.02	0.03	0.04	0.05	0.06	0.07	0.08	0.09	0.1
0	0.53	0.53	0.52	0.59	0.52	0.52	0.52	0.52	0.52	0.52	0.52
0.01	0.38	0.38	0.38	0.38	0.37	0.37	0.37	0.37	0.36	0.36	0.36
0.02	0.32	0.32	0.32	0.31	0.31	0.31	0.30	0.30	0.30	0.29	0.29
0.03	0.28	0.27	0.27	0.26	0.26	0.26	0.25	0.25	0.24	0.24	0.24
0.04	0.24	0.23	0.23	0.22	0.22	0.21	0.21	0.20	0.20	0.20	0.19
0.05	0.20	0.20	0.19	0.19	0.18	0.18	0.17	0.17	0.16	0.16	0.15
0.06	0.17	0.16	0.16	0.15	0.15	0.14	0.14	0.13	0.13	0.12	0.12
0.07	0.14	0.13	0.13	0.12	0.12	0.11	0.11	0.10	0.10	0.09	0.09
0.08	0.11	0.11	0.10	0.10	0.09	0.08	0.08	0.07	0.07	0.06	0.06
0.09	0.09	0.08	0.08	0.07	0.06	0.06	0.05	0.05	0.04	0.04	0.03
0.1	0.06	0.06	0.05	0.05	0.04	0.03	0.03	0.02	0.02	0.01	0.01

| $\bar{P}_{out,max}$ | | | | | | | | | | | |
$\alpha \setminus \beta$	0	0.01	0.02	0.03	0.04	0.05	0.06	0.07	0.08	0.09	0.1
0	51	50	48	47	46	45	43	42	41	40	39
0.01	47	46	44	43	42	41	39	38	37	36	35
0.02	43	41	40	39	38	36	35	34	33	32	31
0.03	39	37	36	35	34	32	31	30	29	28	27
0.04	35	33	32	31	30	28	27	26	25	24	23
0.05	31	29	28	27	26	24	23	22	21	20	19
0.06	27	25	24	23	22	21	19	18	17	16	15
0.07	23	21	20	19	18	17	16	15	14	13	12
0.08	19	18	16	15	14	13	12	11	10	9	8
0.09	15	14	13	11	10	9	8	7	6	5	4
0.1	11	10	9	8	7	6	5	4	3	2	1

Appendix B. Convergence to the true pareto front

Once the optimum geometric configuration for the PTES has been found, a more exhaustive search for the Pareto front is in place. The random search is refined and an objective convergence criteria is needed. Here these two problems are explained with more detail. Since all functions have monotonic behaviours or present only one extreme point no genetic algorithm are needed.

According to the algorithm introduced in Section 3.1 a first step is a random search in the physically acceptable region, from these points the non-dominated points are obtained. In Fig. B.16a this first generation is displayed. A refinement in the algorithm is to enclose the optimal set in two disconnected regions (the minimum rectangular covers), whose areas are increased in order to not miss additional non dominated points. In each step the extension of the covers decrease. For illustrative purposes the output from the 21st iteration is depicted in Fig. B.16b.

As stated above, a convergence criterion is required to acknowledge that the obtained Pareto front is close enough to the real Pareto front. For this purpose the distributions of the round-trip efficiency is used. Since Φ is restricted in the interval $(0, 1)$ a probability distribution is built using a partition of 300 equal sub-intervals (300 bins). In each iteration the entropy of this distribution, P_i, with $i = 1, \ldots, 300$ is

calculated. The Kullback–Leibler divergence, D_{KL}, or entropy divergence gives a measure of the difference in information between two distributions. When comparing the distribution of iteration j with the next one, $j+1$, a measure of how much information is gained from the last iteration, then, as the algorithm approaches to the true Pareto front the distributions converge and the KLD should tend to zero. In this case

$$D_{KL} = \sum_{i=1}^{300} P_i \, Ln \left(\frac{P_i}{Q_i} \right) \qquad (B.1)$$

where Q_i and P_i are the probabilities in the j and the $j+1$ iterations, respectively. In the present analysis it has been used a reliable threshold value of 5×10^{-5}. In Fig. B.16 it is shown that this algorithm converge quickly, after 35 iterations the threshold has been reached.

Appendix C. Comparison between the optimum scale factor of mass flow and the extreme limits $\Gamma = \{0, 1\}$

For completeness, in order to face the benefit from obtaining an optimum scale factor between the heats capacities of the working fluid and those of the thermal reservoirs, which lastly depend on the mass flow scale, here the outcome for two extreme cases are presented for $\bar{P}_{out,max}$, η_{max} and Φ_{max}: $\Gamma_{H,L}^{HE} \to 1$ and $\Gamma_{H,L}^{HE} \to 0$. See Tables C.9 and C.10 and compare with Tables 5–7. This will work as a reference frame in the extremal situations of system–reservoir mass flow ratios.

References

[1] A.B. Gallo, J.R. Simoes-Moreira, H.K. Costa, M.M. Santos, E. Moutinho dos Santos, Energy storage in the energy transition context: A technology review, Renew. Sustain. Energy Rev. 65 (2016) 800–822, http://dx.doi.org/10.1016/j.rser.2016.07.028.

[2] X. Luo, J. Wang, M. Dooner, J. Clarke, Overview of current development in electrical energy storage technologies and the application potential in power system operation, Appl. Energy 137 (2015) 511–536, http://dx.doi.org/10.1016/j.apenergy.2014.09.081.

[3] M.C. Argyrou, P. Christodoulides, S.A. Kalogirou, Energy storage for electricity generation and related processes: Technologies appraisal and grid scale applications, Renew. Sustain. Energy Rev. 94 (2018) 804–821, http://dx.doi.org/10.1016/j.rser.2018.06.044.

[4] Z. Wan, J. Wei, M.A. Qaisrani, J. Fang, N. Tu, Evaluation on thermal and mechanical performance of the hot tank in the two-tank molten salt heat storage system, Appl. Therm. Eng. 167 (2020) 114775, http://dx.doi.org/10.1016/j.applthermaleng.2019.114775.

[5] A. Benato, A. Stoppato, Heat transfer fluid and material selection for an innovative Pumped Thermal Electricity Storage system, Energy 147 (2018) 155–168, http://dx.doi.org/10.1016/j.energy.2018.01.045.

[6] J.D. McTigue, C.N. Markides, A.J. White, Performance response of packed bed thermal storage to cycle duration perturbations, J. Energy Storage 19 (2018) 379–392, http://dx.doi.org/10.1016/j.est.2018.08.016.

[7] A. White, J. McTigue, C. Markides, Wave propagation and thermodynamic losses in packed-bed thermal reservoirs for energy storage, Appl. Energy 130 (2014) 648–657, http://dx.doi.org/10.1016/j.apenergy.2014.02.071.

[8] A. Benato, F. De Vanna, E. Gallo, A. Stoppato, G. Cavazzini, TES-PD: A fast and reliable numerical model to predict the performance of thermal reservoir for electricity energy storage units, Fluids 6 (2021) 256, http://dx.doi.org/10.3390/fluids6070256.

[9] A. Benato, A. Stoppato, Pumped thermal electricity storage: A technology overview, Therm. Sci. Eng. Prog. 6 (2018) 301–315, http://dx.doi.org/10.1016/j.tsep.2018.01.017.

[10] A.H. Hassan, L. O'Donoghue, V. Sánchez-Canales, J.M. Corberán, J. Payá, H. Jockenhöfer, Thermodynamic analysis of high-temperature pumped thermal energy storage systems: Refrigerant selection, performance and limitations, Energy Rep. 6 (2020) 147–159, http://dx.doi.org/10.1016/j.egyr.2020.05.010.

[11] C.S. Turchi, J. Vidal, M. Bauer, Molten salt power towers operating at 600-650: Salt selection and cost benefits, Sol. Energy 164 (2018) 38–46, http://dx.doi.org/10.1016/j.solener.2018.01.063.

[12] N. Peger, T. Bauer, C. Martin, M. Eck, A. Wörner, Thermal energy storage: overview and specific insight into nitrate salts for sensible and latent heat storage, J. Nanotechnol. 6 (2015) 1487–1497, http://dx.doi.org/10.3762/bjnano.6.154.

[13] R.B. Laughlin, Pumped thermal grid storage with heat exchange, J. Renew. Sustain. Energy 9 (2017) 1–16, http://dx.doi.org/10.1063/1.4994054.

[14] Axel Dietrich, Assessment of Pumped Heat Electricity Storage Systems through Exergoeconomic Analyses (Ph.D. thesis), Technishe Universitat Darmstadt, 2017.

[15] T.R. Davenne, B.M. Peters, An analysis of pumped thermal energy storage with de-coupled thermal storages, Front. Energy Res. 8 (2020) 160, http://dx.doi.org/10.3389/fenrg.2020.00160.

[16] L. Wan, X. Lin, L. Chai, L. Peng, D. Yu, J. Liu, H. Chen, Unbalanced mass flow rate of packed bet thermal energy stoorage and its influence on the joule-brayton based pumped thermal electricity storage, Energy Convers. Manage. 185 (2019) 593–602, http://dx.doi.org/10.1016/j.enconman.2019.02.022.

[17] J.D. McTigue, A.J. White, C.N. Markides, Parametric studies and optimisation of pumped thermal electricity storage, Appl. Energy 137 (2015) 800–811, http://dx.doi.org/10.1016/j.apenergy.2014.08.039.

[18] L. Wan, X. Lin, L. Chai, L. Peng, D. Yu, H. Chen, Cyclic transient behavior of the joule-brayton based pumped heat electricity storage: Modeling and analysis, Renew. Sustain. Energy Rev. 111 (2019) 523–534, http://dx.doi.org/10.1016/j.rser.2019.03.056.

[19] R. Fernandez, R. Chacartegui, A. Becerra, B. Calderon, M. Carvalho, Transcritical carbon dioxide charge–discharge energy storage with integration of solar energy, J. Sustain. Dev. Energy Water Environ. Syst. 7 (2019) 444–465, http://dx.doi.org/10.13044/j.sdewes.d6.0235.

[20] A. Thess, Thermodynamic efficiency of pumped heat electricity storage, Phys. Rev. Lett. 111 (2013) 110602, http://dx.doi.org/10.1103/PhysRevLett.111.110602.

[21] J. Chen, J. Guo, Comment on thermodynamic efficiency of pumped heat electricity storage, Phys. Rev. Lett. 116 (2016) 158901, http://dx.doi.org/10.1103/PhysRevLett.116.158901.

[22] J. Guo, H. Yang, B. Lin, Performance characteristics and parametric optimization of weak dissipative pumped thermal electricity storage system, Energy Convers. Manage. 157 (2018) 527–535, http://dx.doi.org/10.1016/j.enconman.2017.12.031.

[23] J. Guo, L. Cai, J. Chen, Y. Zhou, Performance evaluation and parametric choice criteria of a Brayton pumped thermal electricity storage system, Energy 113 (2016) 693–701, http://dx.doi.org/10.1016/j.energy.2016.07.080.

[24] J. Guo, L. Cai, J. Chen, Y. Zhou, Performance optimization and comparison of pumped thermal and pumped cryogenic electricity storage system, Energy 106 (2016) 260–269, http://dx.doi.org/10.1016/j.energy.2016.03.053.

[25] Y. Zhang, Z. Yang, Comparative study on optimized round-trip efficiency of pumped thermal and pumped cryogenic electricity storages, Energy Convers. Manage. 238 (2021) 114182, http://dx.doi.org/10.1016/j.enconman.2021.114182.

[26] Y. Zhao, M. Liu, J. Song, C. Wang, J. Yan, C.N. Markides, Advanced exergy analysis of a Joule-Brayton pumped thermal electricity storage system with liquid-phase storage, Energy Convers. Manage. 231 (2021) 113867, http://dx.doi.org/10.1016/j.enconman.2021.113867.

[27] S. Anvari, O. Mahian, E. Solomin, S. Wongwises, U. Desideri, Multi-objective optimization of a proposed multi-generation cycle based on Pareto diagrams: Performance improvement, cost reduction, and CO2 emissions, Sustain. Energy Technol. Assess. 45 (2021) 101197, http://dx.doi.org/10.1016/j.seta.2021.101197.

[28] G. Francesco Frate, L. Ferrari, U. Desideri, Multi-criteria investigation of a pumped thermal electricity storage (PTES) system with thermal integration and sensible heat storage, Energy Convers. Manage. 208 (2020) 112530, http://dx.doi.org/10.1016/j.enconman.2020.112530.

[29] D. Salomone-González, J. González-Ayala, A. Medina, J.M.M. Roco, P. Curto-Risso, A. Calvo Hernández, Pumped heat energy storage with liquid media: Thermodynamic assessment by a Brayton-like model, Energy Convers. Manage. 226 (2020) 113540, http://dx.doi.org/10.1016/j.enconman.2020.113540.

[30] A.K. Araujo, G.I. Medina, Analysis of the effects of climatic conditions, loading level and operating temperature on the heat losses of two-tank thermal storage systems in CSP, Sol. Energy 176 (2018) 358–369, http://dx.doi.org/10.1016/j.solener.2018.10.020.

[31] K. Deb, Multi-Objective Optimization using Evolutionary Algorithms, John Wiley & Sons, Inc., New York, ISBN: 978-0-471-87339-6, 2001.

[32] J. González-Ayala, J. Guo, A. Medina, J.M.M. Roco, A. Calvo Hernández, Optimization induced by stability and the role of limited control near a steady state, Phys. Rev. E 100 (2019) 062128, http://dx.doi.org/10.1103/PhysRevE.100.062128.

[33] J. González-Ayala, J. Guo, A. Medina, J.M.M. Roco, A. Calvo Hernández, Energetic self-optimization induced by stability in low-dissipation heat engines, Phys. Rev. Lett. 124 (2020) 050603, http://dx.doi.org/10.1103/PhysRevLett.124.050603.

[34] S. Kullback, R.A. Leibler, On information and sufficiency, Ann. Math. Stat. 22 (1951) 79–86, http://dx.doi.org/10.1214/aoms/1177729694.